Effects of hydrogen related defects on the electrical properties of thin film MgO

B. V. Agustsson

RH-15-2006

Björn Víkingur Ágústsson
bjornvikingur@gmail.com
Science Institute, University of Iceland
Dunhagi 3, IS-107 Reykjavik

October 2006

Effects of hydrogen related defects on the electrical properties of thin film MgO

BJÖRN VÍKINGUR ÁGÚSTSSON

Abstract

The effects of hydrogen impurities on the electrical properties of thin film magnesium oxide (MgO) was investigated. Thin MgO films were grown in a reactive magnetron sputtering discharge while hydrogen was added to the growth environment. Nuclear resonance reaction analysis (NRRA), X—ray diffraction (XRD), and impedance spectroscopy measurements were performed on the samples.

The NRRA measurements showed no increase in the hydrogen content of the grown MgO films, as the hydrogen partial pressure was increased in the growth chamber. This may indicate that the amount of hydrogen when the base pressure is in the vicinity of 1×10^{-8} Torr, is sufficient to saturate the MgO crystal. The X—ray diffraction measurements showed polycrystalline structure of the grown films. The MgO films had both (2 0 0) and (2 2 0) crystal planes. The impedance spectroscopy measurements indicated significant electrical conduction in some of the samples. However, the conduction seems to be unrelated to hydrogen flow in to the growth chamber while growth takes place. The large effective size of the capacitors is believed to be the most likely cause for defects at the interface between the $Cr_x Mo_{1-x}$ and the MgO films. Storing the MgO films in ambient air at room temperature for one month resulted in much lower resistance of the films. The film properties were not recovered by annealing.

Acknowledgements

Contents

Chapter 1

Introduction

Magnesium oxide (MgO) is an ionic oxide and a good electrical insulator. MgO thin films are used in numerous applications such as tunneling barrier in magnetic tunneling junctions (Yamano et al., 1993; Kerber et al., 1989; Yuasa et al., 2004; Parkin et al., 2004), in plasma display panels as surface protective layer for dielectric materials to enhance the lifetime and to reduce the firing and sustaining voltage (Choi and Kim, 2004; Cheng et al., 2004; Matsuda et al., 2004), and as buffer layers for high T_c oxide superconductors (Tanaka et al., 1991; Soto et al., 1997). Here we intend to investigate MgO thin films as electrical insulators between ultrathin metallic conductors and see if increased hydrogen partial pressure in the growth environment influences its electrical properties.

To grow MgO thin films two methods are mainly used, molecular beam epitaxy (MBE) (Chambers et al., 1995) or some form of sputtering. One form of sputtering is reactive magnetron sputtering. This method can be used to grow MgO from a magnesium target. Then a magnesium target is sputtered in an oxygen rich environment. By growing Cr_xMo_{1-x} on the MgO substrate we accomplished clear boundary between the grown MgO and the MgO substrate and good lattice matching between Cr_xMo_{1-x} and MgO is achieved when x is equal or close to 0.70, which results in very little strain between the grown films (Chambers et al., 1995; Gylfason et al., 2006).

1

In a high vacuum system the base pressure is manly caused by water (H_2O) and therefore hydrogen is always present in the growth environment. Because of the hydrogen impurities in the growth chamber, hydrogen can be incorporated into the grown film and can thus change its properties. As an example it has been shown that hydrogen can lead to conduction in some wide gap oxides such as SnO_2 (Samson and Fonstad, 1973) and ZnO (de Walle, 2000). Furthermore it has an effect on the refractive index and chemical stability of alumina thin films (Schneider et al., 1999), and is decisive for composition as well as the microstructure evolution of $SrTiO_3$ layers (Schneider et al., 1999). Kiliç and Zunger (2002) made calculations on n–type doping of oxides by hydrogen. Their results indicated that distinction between H as an n–type dopant and as a nondoping impurity depends on whether the hydrogen pinning level is above the conduction band minimum (CBM) of the material (doping) or below the CBM of the material (nondoping). The pinning level is when impurities such as hydrogen have pinned down the Fermi level at the surface and at the substrate–epilayer interface, which then affects the conduction in the material. The hydrogen pinning level for all oxides is located approximately at (3.0 ± 0.4) eV below the vacuum level. According to calculations by Kiliç and Zunger (2002) the hydrogen pinning level for MgO is located at 1.37 eV below CBM and therefore, hydrogen is not an n–doping impurity in MgO. However, Agustsson (2005, p. 59) found some evidence that hydrogen could possibly be the cause of conduction in MgO grown by reactive magnetron sputtering.

In the following chapters the effect of hydrogen related defects on the electrical properties of MgO dielectrics are investigated. Chapter 2 discusses the growth method applied to this study, reactive magnetron sputtering, and the characterization methods used, nuclear resonance reaction analysis (NRRA), X–ray diffraction (XRD), and impedance spectroscopy. Furthermore, the earlier work on the electrical properties of thin film and bulk MgO is summarized. Finally possible defects caused by hydrogen are discussed. Chapter 3 discusses the sample preparation. The results of the XRD, the NRRA, and the electrical measurements are discussed in

chapter 4.

Chapter 2

Growth and characterization of MgO

The MgO thin films used in this study were grown in an asymmetric bipolar pulsed reactive magnetron sputtering discharge. The magnetron sputtering discharge applied to this study was custom designed and has three sputtering guns. The sputtering targets used in this study were Cr, Mo and Mg. Thus it allows for the growth of alloys as well as reactive sputtering. The magnetron sputtering system used is shown in figure 2.1. Three different types of measurements were performed on the samples; electrical impedance spectroscopy measurements, X–ray diffraction (XRD) to explore the crystallinity of the films, and nuclear resonance reaction analysis (NRRA) to record the hydrogen concentration in the samples. The NRRA measurement was performed at Uppsala University in Sweden.

In the following sections the methods used for growth and measurments are discussed along with discussions about earlier studies on MgO bulk material and thin films.
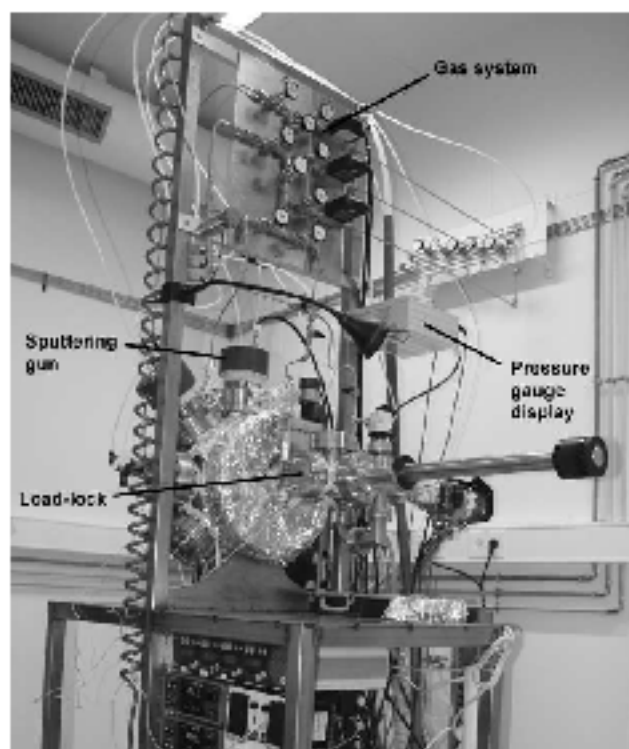
5

Figure 2.1: A photograph showing the magnetron sputtering system used in this study. The system was custom built and has three targets to grow composite materials. Photograph by: Árni Sigurður Ingason.

2.1   Sputtering

Physical vapor deposition (PVD) is a well known method to deposit thin films. A widely used source of vapor is using sputter erosion of solid material by positive ion bombardment. Any material can be volatilized by sputtering and therefore this technique has advantages over other techniques. Furthermore, the deposition rate of the film has been made uniform over large areas (Smith, 1995, p. 432). The ion bombardment is accomplished by using weakly ionized plasma. Plasma is a collection of free particles moving in a random directions and is on the average electrically neutral (Lieberman and Lichtenberg, 1994, p. 6).

A DC glow discharge is shown in figure 2.2. Between the parallel plates there is

a noble gas, typically argon, under low pressure. A voltage source is used to drive current through the low pressure gas between the two electrodes. The gas breaks
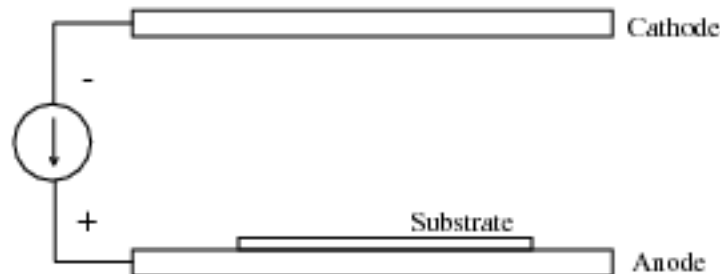

Figure 2.2: A schematic view of a DC glow discharge. The upper electrode is the cathode where the target is placed. The lower electrode is the anode where the substrate for the growth is placed (Lieberman and Lichtenberg, 1994, p. 466).

down and forms a plasma, usually weakly ionized. The discharge is maintained by secondary electron emission from the cathode (Lieberman and Lichtenberg, 1994, p. 457). A voltage of a few thousand volts is required to maintain the discharge.

DC glow discharges have some disadvantages such as high kinetic energy of sputtered particles that can affect the film structures. Its deposition rate is also not acceptable for practical applications. To compensate for these disadvantages a variation of the DC glow discharge has been developed called magnetron sputtering discharge (Chapin, 1974; Waits, 1978), shown in figure 2.3. The difference between the magnetron sputtering discharge and DC glow discharge, shown in figure 2.2, is that magnets are placed behind the cathode. The magnet causes the secondary electrons to be trapped close to the target which results in a higher probability of electron impact ionization and hence higher plasma density (Chapin, 1974). By this modification, it is also possible to grow films at higher current densities, lower voltages, and lower pressures than obtained in a conventional glow discharge.

Magnetron sputtering has been proved to be useful for deposition of conductive films. However, it is also used for deposition of insulating films. It can be done in two different ways. Firstly, by sputtering composite targets and secondly, by adding
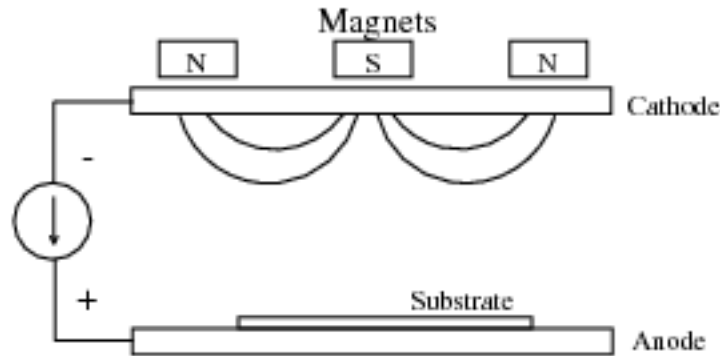
Figure 2.3: A schematic drawing of a DC planar magnetron discharge. A permanent magnet is placed behind the target at the cathode and traps secondary electrons in the electric field (Lieberman and Lichtenberg, 1994, p. 466).

reactive gas into the chamber when sputtered from a metallic target. The gas reacts with the sputtered metal material and forms an insulating layer on the substrate. The second method, referred to as reactive sputtering, has generally lower target fabrication cost and increases target purity compared to using a compound target (Smith, 1995, p. 480). By reactive sputtering it is possible to deposit dielectrics such as oxides and nitrides, as well as carbides and silicides depending on the reactive gas (Lieberman and Lichtenberg, 1994, p. 525). The growth taking place can be divided into two different modes, compound and metal mode with a transition between modes that exhibits hysteresis as shown in figure 2.4. Compound mode occurs when the reactive gas flux is high and the metal ion flux is low, when growing in metallic mode the opposite takes place (Lieberman and Lichtenberg, 1994, p. 525). The hysteresis behavior makes reactive sputtering a very complex process. However, a model that describes the processes taking place has been developed (Berg et al., 1987; Berg and Nyberg, 2005).

When compounds are formed they will not only be deposited on the substrate but also onto the whole chamber including the target. Formation of a thin insulating layer on the target surface is referred to as poisoning. The insulating thin film that forms on the target surface can be thought of as a dielectric of a capacitor where
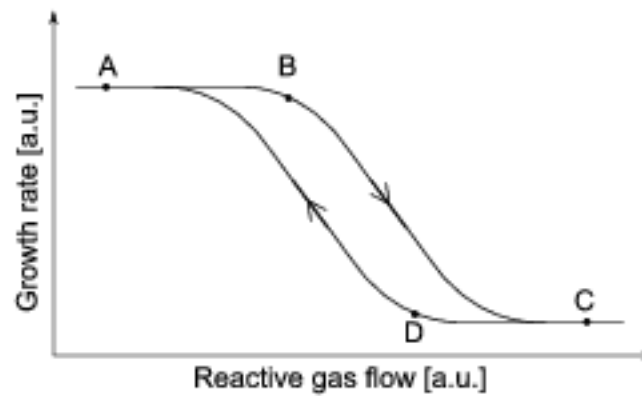
Figure 2.4: When a sputtering is taking place in a pure Ar ambient (point A) the sputtering rate is high. While the flow of the reactive gas is increased the rate remains high until the gas adsorption rate on the target exceeds the sputtering rate (point B). The sputtering rate drops because of poisoning of the target (point C). By lowering the reactive gas flow the poisoning remains until the sputtering rate begins to exceed the adsorption rate (point D) and at last the target is cleaned and metal mode is reached again (point A). After Smith (1995, p. 480).

the target acts as one electrode and the plasma as the other. This is demonstrated in figure 2.5. This results in two problems. Firstly, the current flow is caused by

Figure 2.5: Illustration of how a capacitor is formed when a target is poisoned during reactive sputtering. Plasma and the target acts as conducting electrodes and between is the dielectric. This can cause dielectric breakdown. After Sellers (1998).

ions and because of the dielectric layer the ions are not able to hit the target and therefore no sputtering can occur. Secondly, the capacitor may not have enough

dielectric capability to charge all the way up to the applied voltage. If not, the breakdown of the insulator will cause a sudden release of charge carriers, forcing the local current density to increase into the arc discharge region, which results in arcing (Sellers, 1998). Arcing can be divided into two groups, micro and hard arcing. Hard arcs are generally considered to be a discharge which takes place between a region on the cathode and an earthed surface, whereas microarcs are discharges between different sites on the cathode. While microarcs can normally be tolerated, hard arc events are extremely detrimental to the deposition process (Schiller et al., 1993; Kelly and Arnell, 1999).

To suppress arcing an asymmetric pulsed power supply unit has been introduced. In figure 2.6 a schematic plot of asymmetric bipolar pulse is shown. To adjust the pulse its reverse voltage, pulse frequency, and duty factor can be varied. But duty factor is the relative proportion of the pulse cycle made up of the pulse on period when the target voltage is negative and sputtering is occurring. Kelly et al. (2000)
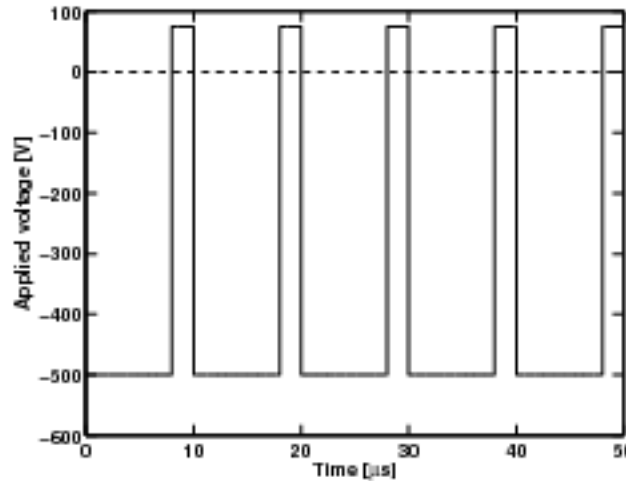

Figure 2.6: A typical waveform of the applied voltage in an asymmetric bipolar pulsed magnetron sputtering discharge. Sputtering takes place when the applied voltage is negative. The positive voltage discharges the target and prevents charge buildup.

showed that there is a strong relationship between the duty factor and the occurring

of hard arcs, and with lower duty factor arcing will be significantly reduced. It has also been shown for growing of alumina films a duty factor of 70% or lower, independent of pulse frequency, is needed for arc suppression (Kelly et al., 2000). Pulse frequency is usually chosen between 20–100 kHz and reverse voltage, that is the amplitude of the positive pulse, is often chosen to be around 10–20 % of the negative operating voltage. A care must been taken to have the reverse voltage low enough not to generate back sputtering, and high enough to maintain preferential sputtering. Sellers (1998) showed that 75–100 V would be effective and safe, and also that returning to forward current as quickly as possible after a reverse bias is critical to maximize the deposition rate.

For reactive sputtering different temperatures can be chosen when growing the films. The growth temperature has an effect on some of the film properties such as roughness, where the surface mobility of the atoms changes with temperature, and the impurity content, but with higher temperatures the growth rate increases and thereby less incorporation of impurities in the film. As an example relevant to this work it has been reported by Aboelfotoh et al. (1977) that the amount of hydroxyl groups in MgO grown at 200 °C is less than the amount grown at room temperature. When the base pressure in their chamber was from 1×10^{-7} to 4×10^{-6} Torr.

2.2 Nuclear resonant reaction analysis

Nuclear resonant reaction analysis (NRRA) is a powerful nondestructive way of studying hydrogen concentration and hydrogen depth distribution in a solid. It typically involves the use of light and heavy elements, and the nuclear reactions characterized by cross sections with narrow widths and large ratios of peak to off-resonant cross sections (Briere, 1993, p. 9). Some different nuclear reactions have been used for the hydrogen profiling such as $^1\text{H}(^{19}\text{F}, \alpha\gamma)^{16}\text{O}$ with a resonance energy of 16.44 MeV or a resonance energy of 6.42 MeV. Another possibility is to use the reaction of $^1\text{H}(^{15}\text{N}, \alpha\gamma)^{12}\text{C}$ and resonance energy of 13.35 MeV or 6.384 MeV (Xiong

et al., 1987). The γ–ray yield from the reaction is then used to determine the hydrogen concentration in the sample. The former has γ–ray yield that is about ten times higher than the latter one and therefore greater sensitivity is achieved but with loss of resolution (Ziegler et al., 1978). The latter reaction (resonance energy 6.384 MeV) has gained popularity due to its small full width of 1.8 keV, excellent peak to background ratio and its relatively easy accessibility. The reaction taking place can be described by the equation (Briere, 1993, p. 9).

$$H + {}^{15}N \ (6.384 \ \text{MeV}) \rightarrow {}^{12}C + \alpha + \gamma \ (4.43 \ \text{MeV}) \tag{2.1}$$
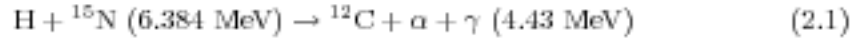
With this method a resolution of 5–10 nm and a sensitivity better than one part per thousand can be reached (Lanford and Rand, 1978).

To find the hydrogen concentration on the surface, the sample is bombarded with 6.384 MeV ^{15}N beam which yields an α particle (^{4}He) and a characteristic 4.43 MeV γ–ray. The energy of the α particle is only 0.5 MeV and therefore it is not useful in the measurements, except for the thinnest free standing films (Briere, 1993, p. 9). The concentration of hydrogen is proportional to the γ–ray count and by detecting them the concentration of hydrogen can be found. Because the resonant reaction occurs at 6.384 MeV it is possible to increase the energy of the incident ^{15}N beam to get deeper into the sample. The beam will then loose energy while penetrating the sample and at certain depth the beam energy has fallen down to the resonant energy and the concentration at that depth can be measured (Lanford et al., 1976). The further the beam goes into the sample the resonant widths increases and therefore the depth resolution decreases. This is due to incident beam energy straggling and is a limiting factor for the depth resolution (Xiong et al., 1987).

2.3   Admittance spectroscopy

For the admittance spectroscopy measurement, a four point probe technique was used when measured at room temperature, but a two point probe measurement was used when the sample was cooled down. In a four point probe measurement (figure

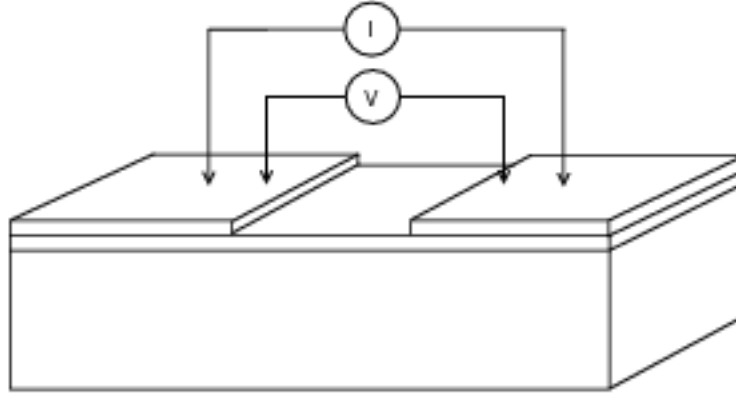2.7) constant current is driven through the sample and the voltage drop over the

Figure 2.7: Four point probe resistance measurement setup. A constant current is passed between the two outer contacts, and the voltage is measured between the two inner contacts.

sample is measured. Because of the high input impedance, the voltmeter will draw very little or no current and therefore the contacts to the sample will have little or no effects at all on the measured value. For the measurements, Signatone coaxial probes connected to a HP4284 LCR meter were used. To measure the impedance of the samples at different temperatures a Janis Research VPF-475 cryostat and a Lake Shore 331 temperature controller were used. The samples were cooled down to 78 K with liquid nitrogen and heated in steps up to 400 K.

The probes used for the two point probe measurement were not screened as those for the four point probe measurement. To see the effects on the phase between two and four point probe measurements, the phases for capacitors 1 and 7 were measured with both techniques at room temperature and are plotted in figures 2.8 and 2.9 respectively. Capacitor 1 had resistance of the order of 10^7 Ω while capacitor 7 had resistance of the order of 10^5 Ω. At high frequencies for capacitor 1 we observe the influence of inductance for the two point probe setup. At the highest frequencies (1 MHz) the phase is close to $-45°$ while measuring with screened cables but when measured with unscreened cables the phase is at $-10°$ at 1 MHz. No difference is

Figure 2.8: The phase of capacitor 1 at room temperature, measured with four point technique and screened cables and two point technique with unscreened cables. The effects of the cables is obvious. Higher inductance in the cables is observed while measuring with unscreened cables. At the highest frequencies (1 MHz) the phase is close to -45° while measuring with screened cables but when measured with unscreened cables the phase is at -10° at 1 MHz.

seen in the phase between two and four point techniques for capacitor 7. At the higher frequencies the phase measured using the two point setup behaves similar to the phase measured using the four point setup.

The total conductivity $\sigma_{tot}(\omega)$ of dielectric films can be written as

$$\sigma_{tot}(\omega) = \sigma_{ac}(\omega) + \sigma_{dc} \tag{2.2}$$

where σ_{dc} is the dc-dependent and $\sigma_{ac}(\omega)$ is the frequency–dependent conductivity. These two conductivities are assumed to be caused by completely different processes with the ac–dependent part taking the form

$$\sigma_{ac}(\omega) = A\omega^s \tag{2.3}$$

for all amorphous semiconductors and insulators. Here A is a temperature dependent constant and s is generally between 0.0 and 1.0 (Elliott, 1978; Ghosh, 1990; Lal
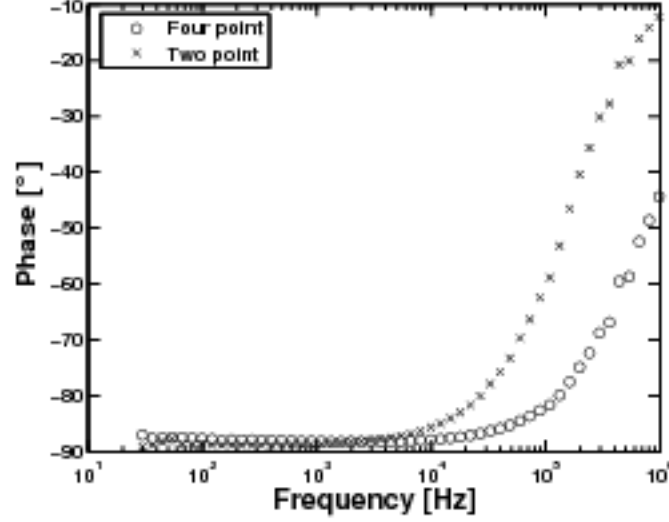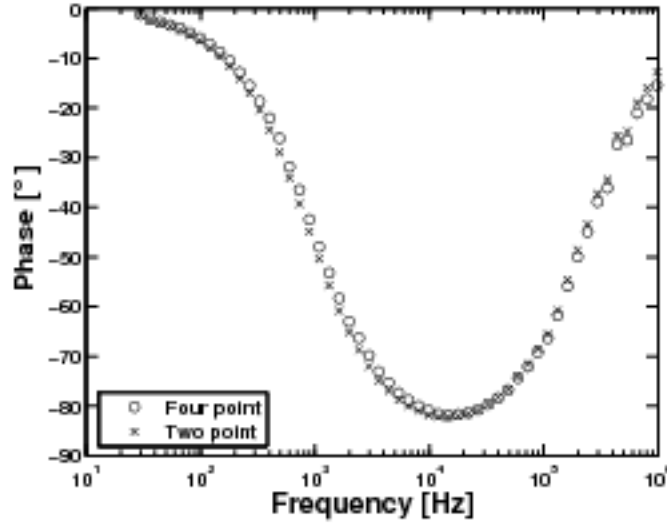
Figure 2.9: The phase of capacitor 7 at room temperature, measured with four point technique and screened cables and two point technique with unscreened cables. The effects of the unscreened cables on the phase of the measurements can be neglected.

et al., 2003). A log–log plot of equation (2.3) where admittance (Y) is on the y–axis and frequency (ω) is on the x–axis can tell us what kind of conduction mechanism is taking place. At low frequencies, where any departures from linearity carries information on the type of the loss mechanism involved, the admittance is not dependent on frequency but at higher frequencies it becomes frequency dependent (Ghosh, 1990).

Two different mechanisms have been proposed for the relaxation mechanism, quantum mechanical tunneling (QMT) and hopping over a barrier (HOB) as well as combinations or variations of those two, where the responsible carriers are atoms or electrons (or polarons) (Ghosh, 1990). A polaron is formed when a moving charge in a crystal with some ionic character polarizes the lattice around it. The lattice polarization then acts as a potential well that hinders the movements of the charge and therefore the mobility is strongly decreased and becomes highly temperature dependent, because the binding energy of the electronic carrier to the

polarized lattice must be overcome (Kingery et al., 1975, p. 870). These charges are considered to move by discontinuous "hopping" or jumps between well localized sites within the solid, but most of the time they are considered to be at rest at these sites. This mechanism must be clearly distinguished from "free band" conduction (Jonscher, 1972).

In HOB, the carrier motion occurs by hopping over the potential barrier separating two defect centers with a height of the potential barrier W, measured form the ground state, which is a random variable. Correlated barrier hopping (CBH) is a variation of HOB which accounts for changes in the s parameter. By assuming a Coulombic correlation between the charged defect centers which results in correlation between W and the intersite separation which is called correlated barrier hopping (Elliott, 1978; Pike, 1972).

The parameter s in equation (2.3) depends on different processes when compared to different models. For the QMT model it is temperature independent but frequency dependent, for simple HOB model the parameter s is predicted to be unity and independent of temperature and frequency, and for the CBH model it decreases with increasing temperature (Elliott, 1978; Ghosh, 1990). The frequency exponent according to CBH is then given by the equation

$$s = 1 - \frac{6k_{\mathrm{B}}T}{W_{\mathrm{m}} + k_{\mathrm{B}}T\ln(\omega\tau_0)} \tag{2.4}$$

where k_{B} is Boltzmann constant, W_{m} is the polaron binding energy, and τ_0 is the characteristic relaxation time (Elliott, 1987).

2.4   Thickness measurements

To estimate thickness of thin films different methods can be used. For ultra thin insulators (<60 Å) or semiconductors, Fowler–Nordheim tunneling measurements can be used. With this method thickness changes of ~ 1 Å can be detected (Zafar et al., 1994, 1995). Other properties of the materials can also be detected with this

method such as barrier heights (Zafar et al., 2002), and the effective electron mass (Zafar et al., 1994).

Another method to determine the thickness of thin films is X–ray reflection. It can be used to determine the film density, the surface roughness as well as determining thicknesses between 2–200 nm with a precision of about 1–3 Å. An X–Ray beam is reflected at the surface of the material under investigation. Above the critical angle, which is usually less than $0.3°$ for most materials, reflections from different interfaces interfere and interference fringes appear. The period of the fringes and the fall in intensity are related to the thickness and the roughness of the layer. As the angle where fringes are visible increases the roughness of the surface decreases (Holý et al., 1999, p. 119).

2.5 X–ray diffraction

Crystals consists of planes of atoms which are spaced a distance d apart. They can be resolved into many atomic planes, each with a different d–spacing. To access the crystal quality and the lattice parameters of the materials X–ray diffraction (XRD) can be used. Depending on the angle of incidence the X–rays bombarding the sample can either pass through the crystal or interact with atoms in the lattice. Because of the phase relation between the scattered X–rays from the atoms in the lattice, interference will occur. Most of the interferences are destructive but in some directions constructive interference takes place and diffracted beams are formed (Cullity, 1978, p. 82).

The scattered rays will be completely in phase (constructive interference) if their path difference is equal to a whole number of wavelengths. This is described by Bragg's law

$$d = \frac{n\lambda}{2\sin\theta} \tag{2.5}$$

where d is the distance between planes, λ is the wavelength, θ is the angle of

incidence, and $n = 1, 2, 3, \ldots$. Different crystal planes can be found by using

$$d = \frac{a_0}{\sqrt{h^2 + k^2 + l^2}} \tag{2.6}$$

which is valid for a cubic crystal. Using equation (2.6) along with the crystal line spacing, d, obtained from the X–ray diffraction it is possible to find the Miller indices (h, k, and l) which describe the crystal planes of the crystal. In equation (2.6) a_0 is the lattice constant of the MgO crystal.

2.6   MgO thin films

Magnesium oxide thin films have been studied by several groups. Soto et al. (1997) report on the growth of MgO thin films by pulsed DC magnetron sputtering on GaAs substrate that had room temperature resistivity of 10^{11} Ωcm, when growth rate was in the range 0.25–3.30 nm/min (0.04–0.55 Å/s). Deposition took place from room temperature to 500 °C where they found that the deposition rate was sensitive to higher temperature, but not the crystallinity. They grew their samples with the oxygen pressure in the range from 1–7.5 % O_2 at a total pressure of 5 mTorr, and the best results were obtained in the lower oxygen content deposition. However, films obtained at a higher oxygen partial pressures in the chamber were more resistant to aging. Hsu and Raj (1992) found however, when MgO films were grown epitaxially on GaAs by reactive rf planar magnetron sputtering, that at lower temperatures, the MgO film was not fully crystalline. However, highly oriented crystalline films were obtained when the substrate temperature ranged from 500 to 530 °C.

Fan et al. (2001) used metal–organic chemical vapor deposition (MOCVD) to produce single–crystalline MgO thin films on MgO (1 0 0), (1 1 0) and (1 1 1) substrates. They claimed that higher concentration of atomic oxygen lead to layer–by–layer growth and thus atomically flat surfaces.

Rakotomiraho et al. (1986) studied some physical properties of thin MgO films which were produced by reactive sputtering. They concluded that conduction in the films was due to electron hopping from a trap level to extended states in the

conduction band and that the ionization energy ($E_i = (1.4 \pm 0.1)$ eV) of the trap levels were due to oxygen vacancies.

Hydration of thin MgO films was reported by Aboelfotoh et al. (1977). As mentioned before they claimed that films deposited at 200 °C had higher hydroxyl content than films deposited at room temperature and the base pressure between 1×10^{-7} to 4×10^{-6} Torr. They also found that films deposited at fast rate ($\sim$7800 Å/min or $\sim$130 Å/s) had less hydroxyl groups than films deposited at slower rate ($\sim$160 Å/min or $\sim$2.67 Å/s) at 200 °C, and that adsorption of residual water on MgO did not influence the growth mode of the grown film. Hydration of MgO thin films should not come as a surprise because water can bind strongly to the MgO surface. This is because high surface charge of MgO and that the lattice parameter of MgO is such that the water molecules can maximize their interaction with the surface and form hydrogen–bond to other water molecules in the monolayer (Engkvist and Stone, 1999). Furthermore, the chemical stability of MgO is such that it can easily absorb moisture and form magnesium hydroxide ($Mg(OH)_2$) (Refson et al., 1995). Mejias et al. (1999) claim that hydrogen reaction can start at a defect site on the MgO single crystal, such as corner, edge and surface. Hydrogen can then be incorporated into the MgO thin films both in the growth environment and when they are subjected to atmosphere. Lee et al. (2003) exposed MgO thin films to 80 % humid ambient at room temperature. Then hydration was formed on the surface of the MgO film and also in the inner part of the film, the entire region was approximately 2 nm thick.

Duriez et al. (1990) studied structural characterization of MgO(100) surfaces. They found that MgO surface which was cleaved in air was damaged irreversibly by water vapor. It created point defects on the surface. The samples were also covered by contamination layer of CO_2 and H_2O which was possible to clean by annealing at 700 °C but the surface defects created by water remained.

Furthermore, the hydration behavior of MgO single crystals and thin films was investigated by Lee et al. (2003). They found that the crystal direction did play

important role in the hydration of the MgO films, where the (111) plane hydrated more than the the (100) plane. Furthermore, the results showed that the grain size and density of the MgO thin films could be crucial factors influencing the hydration. The clusters of $Mg(OH)_2$ appeared to be formed on the surface because of volume expansion as a result of lattice mismatch between MgO and $Mg(OH)_2$. They grew both in vertical and lateral directions and after long–term hydration the growth in hydration clusters in vertical direction was saturated. However, the growth in the lateral direction continued. When looking at the MgO thin films they were hydrated even though it was not done intentionally, and much more hydrated than single crystals with the same orientation (100). This is most likely caused by the existence of grain boundary as mentioned by Mejias et al. (1999) and further the partly exposure of the (111) plane on the surface. The part of the density in the hydration of the inner part of the thin MgO film was also discussed by Lee et al. (2003). The density was found to have very important effect on the diffusion of H_2O through the film where the MgO could react with the hydrogen and form $Mg(OH)_2$.

2.7   Electrical properties of bulk MgO at different temperatures

Measurements of the electrical properties of bulk MgO crystals have been performed by several investigators. Most of those measurements are performed at temperatures which are higher than or around 1200 K (Mitoff, 1961; Osburn and Vest, 1971; Sempolinski et al., 1980) but some measurements have also been performed at lower temperatures, down to 300 K (Lempicki, 1953). Lempicki (1953) did his measurements on bulk MgO from room temperature up to 1500 K. From room temperature up to 800 K he did not get reproducible results. However, the activation energy for the conductivity of the crystal was measured to be between 0.15 and 0.25 eV. Kathrein and Freund (1983) studied the direct current conductivity of MgO single crystals between 500 K to 1200 K. Below 1000 K the activation energy was mea-

sured to be (1.1 ± 0.2) eV but about 2.4 eV at higher temperatures. The mechanism occurring at lower temperatures was proposed to be due to electrons on anion defect sites corresponding to O^- in the O^{2-} structure which were consequence of the presence of carbon and hydrogen in the MgO.

Mitoff (1961) looked at conductivity of single crystals of MgO at temperatures from 1273 to 1773 K. He found that the activation energy obtained form the Arrhenius plots varied between 2.17–3.47 eV [50–80 kcal/mol]. Below 1773 K down to 1273 K all the results indicated that the impurities dominated the electrical conductivity, but analysis of the crystals used, showed several hundred parts per million impurities, principally Ca, Al, Si, and Fe. The conduction in MgO can be divided predominantly into electronic or ionic and the conduction depending on temperature, oxygen pressure and purity of the sample. At the lower temperatures around 1273 K and intermediate oxygen partial pressure ionic conduction was favorable, and at higher temperatures with either low or high oxygen flow electron conduction was more favorable.

Lewis and Wright (1968) investigated MgO single crystals at temperatures in the range 673 K to 1023 K. They concluded that in this temperature range the activation energy was about (2.8 ± 0.1) eV which agrees well with measurements at higher temperatures. They also looked at polycrystalline MgO and saw that the electrical conduction was very much higher than for MgO single–crystals with activation energy of 1.2 eV. They suggest that this difference in activation energy between single–crystals and poly–crystals, could be due to possible thermal ionization of traps at the grain boundaries which would be a possible mechanism for controlling conduction. This would account for the high conductivity of the polycrystalline specimen which contained a large percentage of impurity atoms.

## 2.8 Hydrogen as an impurity in MgO crystals

Freund et al. (1984) looked at how low atomic number impurity atoms (hydrogen and carbon) were incorporated into magnesium oxide and what kind of vacancies

$(\cdot)$	dot: single positive
$(')$	prime: single negative
$('')$	double prime: double negative
$(\times)$	cross: neutral
index i:	interstitial
V''_{Mg}	Mg^{2+} vacancy
$OH^{\cdot}$	OH^{-} substituting for O^{2-}
$O^{\cdot}_{O}$	O^{2-}_2 substituting for two O^{2-}
$O^{\times}$	O^{2-} on O^{2-} lattice site

Table 2.1: List of symbols and specific defect configuration used in the chemical formulas. From Freund et al. (1984).

would be produced in the crystal. According to them, H_2O produces equimolar concentration of extrinsic cation vacancies and OH^{-} ions in the magnesium oxide. The H^{+} cations convert, to a large extent, into molecular H_2 and peroxy ions, O_2^{2-}. Then H_2 may be lost and the peroxy ions are left as excess oxygen in the MgO crystal. The thermal decay of O_2^{2-} above 530 °C generates positive holes, both vacancy–bound and highly mobile unbound O^{-} states, which diffuse toward the surface. This can cause surface charges, and autoxidation of transition–metal impurities in the bulk.

In table 2.1 the symbols used in some of the following chemical formulas are explained. When H_2O dissolves in a MgO crystal it can cause three dominant types of vacancies to be formed, which are half $[OH^{\cdot}V''_{Mg}]'$, fully $[OH^{\cdot}V''_{Mg}HO^{\cdot}]^{\times}$ and over-compensated $[H_i^{\cdot}]$ vacancies. The fully compensated defect is expected to be oriented parallel to the [100] direction of the MgO structure. This is shown at the bottom left hand side of figure 2.10 where the formation of H_2 molecules is illustrated. This formation of H_2 can then be explained by the formula:

$$[OH^{\cdot}V''_{Mg}HO^{\cdot}]^{\times} \rightleftharpoons [^{O^{\cdot}}_{O^{\cdot}}(H_2)''_{Mg}]^{\times} \qquad (2.7)$$
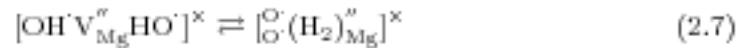
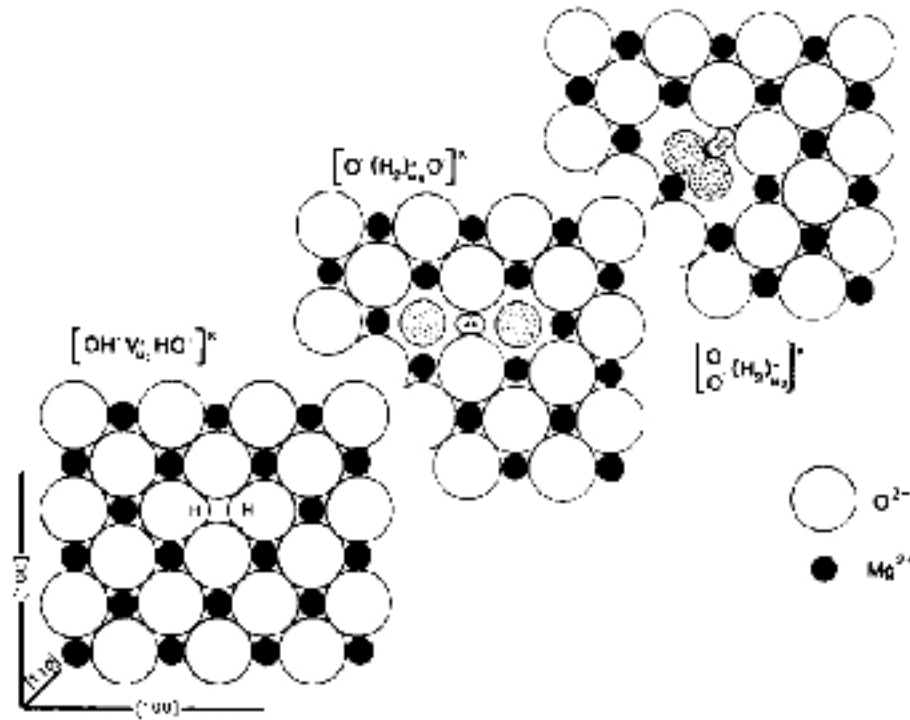But the probability of the $(H_2 + O_2^{2-})$ formation depends on the O–O distance

Figure 2.10: Conversion of the fully OH$^-$–compensated cation vacancy defect in MgO into the (H$_2$ + O$_2^{2-}$) configuration by internal charge transfer. Lattice relaxation due to much smaller O$_2^{2-}$ atom than O^{2-} is not shown. From Freund et al. (1984).

across the cation vacancies (Freund et al., 1984).

Without disorganizing the charge balance in the crystal, H$_2$ can be removed according to the equation:

$$[\substack{O^. \\ O}(H_2)_{Mg}^{''}]^{\times} \rightleftharpoons [\substack{O^. \\ O}V_{Mg}^{''}]^{\times} + (H_2)_i^{\times} \tag{2.8}$$
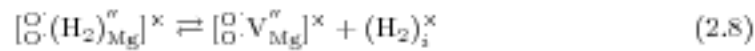
where the hydrogen is left as interstitial and from there it can enter gas phase and then be removed from the crystal at certain temperatures:

$$(H_2)_i^{\times} \leftrightharpoons H_{2(g)} \tag{2.9}$$
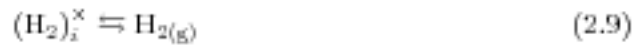
This will then leave the excess oxygen in the form of peroxy ions in the crystal and equimolar concentration of cation vacancies. This however, only happens at relatively high temperatures, between 300 and 550 $^\circ$C (Freund et al., 1984).

2.9   Effects of ion bombardment

When sputtering oxides or oxidized metals high energy negative ions can be produced in the plasma. These ions are then accelerated from the target to the substrate due to negative potential of the target. These atoms can then cause resputtering (back sputtering) of the substrate (Kester and Messier, 1986).

Effects of high–energy atoms have been studied during growth of oxides such as zinc oxide (ZnO) (Tominaga et al., 1981), barium titanate ($BaTiO_3$) (Shintani et al., 1975), indium tin oxides (ITO) (Ishibashi et al., 1990), $YBa_2Cu_3O_x$ (Selinder et al., 1991) and magnesium oxide (MgO) (Hamerich et al., 1994). The effect of ion bombardment on the substrate can influence the thin film properties. Rossnagel and Cuomo (1988) found that the bombardment can cause physical changes in the film and affect other related properties such as electrical resistivity, the dielectric constant and the stability of the film. Tominaga et al. (1981) investigated the influence of high–energy neutral atoms when sputtering zinc oxide (ZnO). They showed that there is a good correlation between the decrease in the deposition rate and the flux of high–energy neutral atoms. Tominaga et al. (1993) observed strong flux of O^- ions and O atoms simultaneously during the sputtering of ZnO target at gas pressures below 1 mTorr. Which confirms that there is a clear influence of the film bombardment by these energetic ions at those gas pressures. Selinder et al. (1991) found that the deposition rate for $YBa_2Cu_3O_x$ decreased at certain oxygen partial pressure where the deposition rate dropped drastically. They also mentioned two ways to reduce the resputtering effect produced by high energetic particles at the substrate. This can be accomplished by either reducing the energy by collisions before these energetic particles reach the substrate, or by reducing the initial energy of the ions by hindering collisionless acceleration in the dark space. The dark space is close to the target where secondary electrons have not had enough inelastic collisions with molecules for the glow from the exited states to be visible (Smith, 1995, p. 472).

Kester and Messier (1986) sputtered some materials and compared their results

to a model which was based on ion potential and electron affinity values of the elements in the sputtering material. For investigation of the samples three methods were used: scanning electron microscope (SEM) micrographs, thickness profile, and visual observation. In their study nine out of fifteen materials sputtered showed clear evidence of resputtering and three materials were probably (two out of three methods showed evidence of resputtering) effected by resputtering.

The deposition process in magnetron sputtering discharge was modeled by Hamerich et al. (1994). By this model the sputtering process for multiconstituent materials which accounts for variations in the deposition rate of thin films sputtered with planar sputtering systems in the face to face geometry was developed. Their model was compared among others materials to MgO, sputtered from a MgO target, and was in excellent agrement with grown films. It showed variations of the refraction index between 1.67 to 1.70. This variation in the refraction index is caused by resputtering and was mainly in a region around the projection of the magnetron ring on the substrate.

Chapter 3

Sample preparation

Three different measurements were performed on the samples. All samples were produced on MgO (1 0 0) substrates. All measurements demanded different sample preparation. In this chapter the sample preparation for these experiments is described along with the treatment of the substrates prior to the film growth and the magnetron sputtering device configuration.

3.1 Reactive sputtering

The substrates used were first cleaned in trichlorethylene, acetone and methanol ultrasonic baths for 5 minutes each, blown dry with N_2 and then heated at 700 °C for 10 minutes in vacuum. The target was an 99.95 % pure Mg metal. In the sputtering process current regulation was used where the current to the Mg target was set to 900 mA. The oxygen was delivered to the sample through a pipe that was placed close to the sample holder. In figure 3.1 the oxygen inlet and the substrate holder are shown. The oxygen flow was fixed at 1.1 sccm and the argon flow was kept constant at 40 sccm. Asymmetric pulsed DC magnetron sputtering was applied with 60 kHz frequency, an reverse time of 5 μs (70 % duty factor), and the reverse voltage was 20 % of the applied voltage.
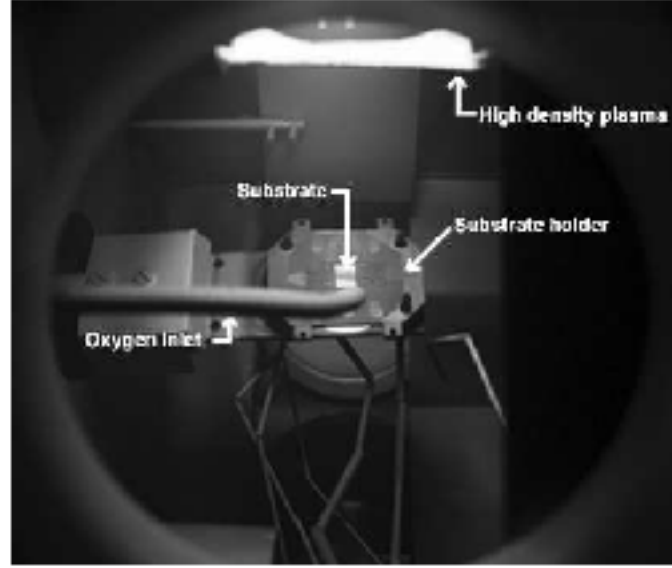
Figure 3.1: The sample holder in the magnetron sputtering discharge. High density plasma next to the target is seen at the top of the figure. The substrate lies on the substrate holder seen in the center of the figure. A heater is under the substrate holder to control the growth temperature. The pipe where the oxygen was delivered to the sample can be seen in front of the substrate holder. Photograph: Árni Sigurður Ingason.

3.2   Hydrogen incorporation

As mentioned before most of the base pressure in a growth chamber is caused by water, and therefore significant amount of hydrogen is expected to be present while growing a film. Hydrogen will therefore be incorporated into the grown film. It is possible to estimate the growth rate of one monolayer of impurities and compare it to the film deposition rate. As first assumption the base pressure is only caused by hydrogen (the base pressure is mainly caused by water), the time to grow one monolayer of hydrogen can be calculated (Sze, 2002, p. 359)

$$t = \frac{N_s\sqrt{MT}}{2.62 \times 10^{20} p} \tag{3.1}$$

where N_s is the number of molecules per unit area, M is the molecular weight, T is temperature in Kelvin and p is the pressure in Pa. The amount of hydrogen in

a grown film will therefore be dependent on the film growth rate. In this study, instead of changing the growth rate to get more hydrogen incorporated into the film, hydrogen was intentionally added into the chamber and the growth rate was held constant. The amount of hydrogen was changed from 0.00–1.33 sccm in steps. The higher value of the hydrogen flow (1.33 sccm) was the highest flow rate that allowed growth in metal–mode. To control the hydrogen (H_2) flow an Aera FC7700C mass flow controller was used. This controller was calibrated for nitrogen (N_2) but according to manufactures the H_2 conversion factor for N_2 is 1.010, i.e. 100 sccm flow of N_2 results in 101 sccm flow of H_2.

3.3 Samples for nuclear resonance reaction analysis

Samples for nuclear resonance reaction analysis (NRRA) measurements were prepared on a MgO substrate. The substrate was electrically floating. The base pressure in the chamber was ranging from 8.8×10^{-6} to 2.9×10^{-5} mTorr. The substrate was coated with a Cr_xMo_{1-x} alloy of thickness close to 150 Å at 200 °C to get an interface between the substrate and the grown MgO film. The Cr_xMo_{1-x} film was grown at a growth rate of 0.49 Å/s. Then about 3000 Å thick film of MgO was grown at temperature of 500 °C at the rate of 0.45 Å/s, with the growth pressure of 2.87 mTorr. The MgO film was grown from a Mg target and oxygen was supplied close to the substrate. During the growth, hydrogen was added with flow rate in the range from 0.00–1.33 sccm. The Ar flow into the chamber was 40 sccm and the O_2 flow was 1.1 sccm. On top of this structure another Cr_xMo_{1-x} thin film was grown. The thickness of this layer was chosen to be of 200 Å thick, sputtered at temperature 200 °C. In figure 3.2 the structure of the samples is shown. The thickness of the overlaying Cr_xMo_{1-x} film was chosen so that at least two energy steps would be needed for the ^{15}N beam to get through the film. By this the water stuck at the surface of the sample should not effect the measured hydrogen concentration of the sample. Exact growth parameters for the samples are given in table 3.1.
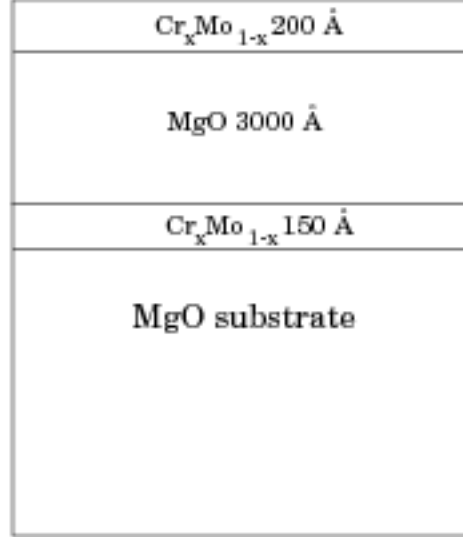
Cr_xMo_{1-x} 200 Å

MgO 3000 Å

Cr_xMo_{1-x} 150 Å

MgO substrate

Figure 3.2: The structure of the samples used for nuclear resonance reaction analysis (NRRA).

	Sample 1	Sample 2	Sample 3	Sample 4	Sample 5
Base pressure [Torr]	2.93×10^{-8}	2.21×10^{-8}	8.78×10^{-9}	1.73×10^{-8}	1.79×10^{-8}
Growth pressure [Torr]	2.86×10^{-3}	2.84×10^{-3}	2.85×10^{-3}	2.87×10^{-3}	2.89×10^{-3}
H_2 flow [sccm]	0.00	0.20	0.40	0.53	1.33
H_2 partial pressure [Torr]	0.00	1.39×10^{-5}	2.77×10^{-5}	3.62×10^{-5}	9.08×10^{-5}
O_2 partial pressure [Torr]	7.65×10^{-5}	7.56×10^{-5}	7.55×10^{-5}	7.58×10^{-5}	7.49×10^{-5}

Table 3.1: Growth parameters for the samples that were made for the nuclear resonance reaction analysis (NRRA). For all the samples an MgO (1 0 0) substrate was used with approximately 150 Å thick Cr_xMo_{1-x} film on top. At a oxygen flow of 1.1 sccm, the growth rate of MgO was around 0.45 Å/s. Approximately 3000 Å thick MgO film was grown on top of the Cr_xMo_{1-x} layer. On top of the MgO thin film approximately 200 Å thick Cr_xMo_{1-x} film was grown. The H_2 partial pressure was calculated by dividing the H_2 flow by the total flow of gases into the chamber. This explains the zero H_2 partial pressure for the first sample even though hydrogen exists in the chamber as can be seen from the base pressure which mainly consists of water.

3.4 Capacitors grown by reactive magnetron sputtering

For investigation of the electrical properties of the MgO thin films, capacitors were produced using shadow masks, and their structure is shown in figure 3.3. A Cr_xMo_{1-x} film was grown on the MgO substrate. An MgO thin film was grown
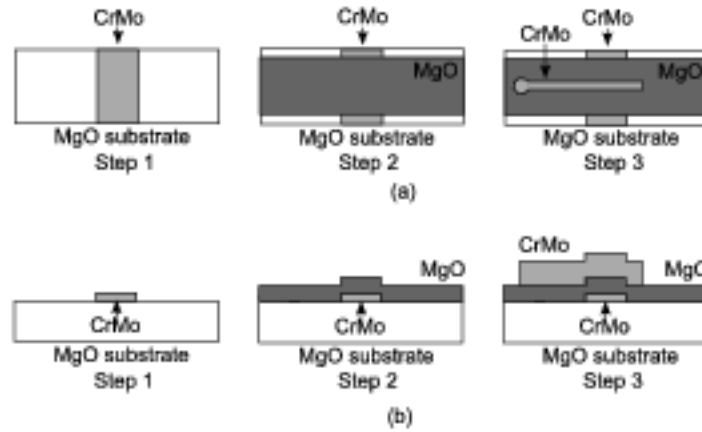

Figure 3.3: The steps of the capacitor fabrication. Figures (a) and (b) show top view and side view of the capacitor respectively. In step one approximately 15 Å thick Cr_xMo_{1-x} film was sputtered on the MgO substrate. In step two 1000 Å MgO film was sputtered on top of the Cr_xMo_{1-x} layer. In step 3, 1040 Å thick Cr_xMo_{1-x} contact was grown on top of the MgO film. From Agustsson (2005).

from a metallic target while oxygen gas was supplied to the sample. The substrate was electrically floating during growth. The growth rate of the MgO film was 0.34 Å/s. Several samples were prepared with different hydrogen flow supplied into the chamber ranging from 0.00 to 1.33 sccm of hydrogen. On top of this layer another film of Cr_xMo_{1-x} was grown. Both Cr_xMo_{1-x} films were sputtered at 200 °C. The underlying film was around 150 Å thick and the overlying film around 1040 Å. MgO was grown at 300 °C which resulted in a polycrystalline film around 1000 Å thick.

3.5   Samples for the X–ray diffraction

Samples for the X–ray diffraction (XRD) were grown, as for the other samples, on top of a MgO (1 0 0) substrate. First 600 Å Cr_xMo_{1-x} film was grown at the growth rate of 0.37 Å/s and on top of that 4000 Å MgO film at the growth rate of 0.54 Å/s were grown. In figure 3.4 the structure of the samples is shown. In table
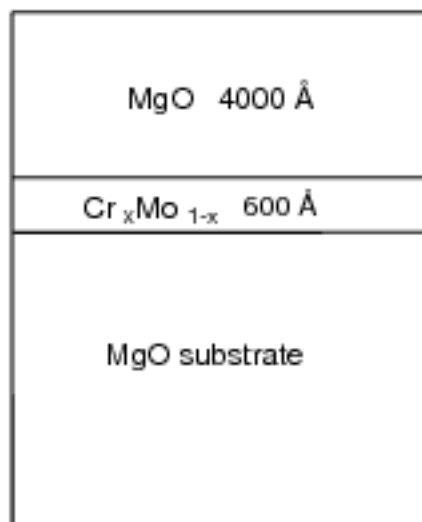
```
+---------------------------------+
|                                 |
|                                 |
|         MgO   4000 Å            |
|                                 |
|                                 |
+---------------------------------+
|     Cr xMo 1-x   600 Å          |
+---------------------------------+
|                                 |
|                                 |
|         MgO substrate           |
|                                 |
|                                 |
|                                 |
+---------------------------------+
```

Figure 3.4: The structure of the samples used for the X–ray diffraction.

3.2 the growth parameters for the samples are shown. During the growth of the Cr_xMo_{1-x} and MgO films the substrate was electrically floating. MgO was grown from a metallic Mg target and oxygen gas was supplied close to the sample at the rate of 0.90 sccm. During the growth of the MgO film hydrogen was intensionally added into the growth chamber. The flow of hydrogen was between 0.00 and 1.33 sccm. The base pressure was ranging from 3.75×10^{-9} to 3.00×10^{-8} Torr and the growth pressure was in the vicinity of 2.75×10^{-3} Torr.

	Sample 1	Sample 2	Sample 3	Sample 4
Base pressure [Torr]	3.00×10^{-8}	6.70×10^{-9}	3.75×10^{-9}	4.45×10^{-9}
Growth pressure [Torr]	2.75×10^{-3}	2.76×10^{-3}	2.73×10^{-3}	2.75×10^{-3}
H_2 flow [sccm]	0.00	0.20	0.40	0.61
H_2 partial pressure [Torr]	0.00	1.36×10^{-5}	2.67×10^{-5}	4.02×10^{-5}
O_2 partial pressure [Torr]	7.37×10^{-5}	6.74×10^{-5}	5.95×10^{-5}	5.97×10^{-5}

	Sample 5	Sample 6	Sample 7
Base pressure [Torr]	1.94×10^{-8}	4.37×10^{-9}	1.11×10^{-8}
Growth pressure [Torr]	2.66×10^{-3}	2.69×10^{-3}	2.70×10^{-3}
H_2 flow [sccm]	0.81	1.01	1.33
H_2 partial pressure [Torr]	5.16×10^{-5}	6.49×10^{-5}	8.50×10^{-5}
O_2 partial pressure [Torr]	5.75×10^{-5}	5.78×10^{-5}	6.38×10^{-5}

Table 3.2: Growth parameters for the samples made for the X–ray diffraction (XRD). First 600 Å thick Cr_xMo_{1-x} film was grown on top of MgO (1 0 0) substrate. On top of the Cr_xMo_{1-x} film 4000 Å thick MgO film was grown. The H_2 partial pressure was calculated by dividing the H_2 flow by the total flow of gases into the chamber. This explains the zero H_2 partial pressure for the first sample even though hydrogen exists in the chamber as can be seen from the base pressure which mainly consists of water.

Chapter 4

Results and discussion

Three types of measurements were performed which required different types of sample preparation as described in the previous chapter. The samples were investigated by nuclear resonance reaction analysis (NRRA) to measure the hydrogen concentration in the MgO films, X–ray diffraction to see the crystal planes, and impedance spectroscopy to investigate the electrical properties and conduction mechanism in the dielectric.

The material stoichiometry in grown compounds does affect its properties. The ratio between magnesium and oxygen, in MgO compounds, is supposed to be 1:1. In this study the ratio was not measured. However, Vuoristo et al. (1991) did RBS measurements on MgO thin films grown by rf magnetron sputtering which had the ratio close to 1:1. In previous studies on MgO thin films grown on Si substrates by pulsed DC reactive magnetron sputtering performed at the University of Iceland, the ratio of Mg versus O measured by RBS was 1:1 (Agustsson, 2005). We assume that this ratio has not changed in the current study.

4.1   Hydrogen concentration in MgO thin films

In section 2.2 the nuclear resonance reaction analysis is discussed. This technique uses a ^{15}N beam which penetrates the measured sample and at 6.384 MeV resonance

35

energy γ particles are produced, these particles can then be used to estimate the hydrogen content in the samples.

For a beam of atoms entering the sample, it is possible to calculate the concentration of hydrogen (atoms/cm^3) with a formula which is given by (Rydén et al., 1989):

$$c_s = c_c \frac{(dE/dx)_s}{(dE/dx)_c} \frac{(N_{\gamma s} - B\Delta t_s)}{(N_{\gamma c} - B\Delta t_c)} \frac{Q_c}{Q_s} \tag{4.1}$$

Where dE/dx is the stopping power of the material, N_γ is the number of γ quanta detected, B is the background contribution per time unit and is mainly due to cosmic radiation, Δt is the measuring time, Q is the ^{15}N dose given to the sample during the measuring time, and c is the concentration of hydrogen in the calibration sample. The subscript s stands for the investigated sample and the subscript c for the calibration sample (Rydén et al., 1989). The sample used for calibration was $TaH_{0.47}$ and was prepared at the Department of Chemistry at Uppsala University. A Van de Graaff tandem accelerator with a terminal voltage of 1.0–5.0 MV and stability of ± 1 kV was used for the measurement. The ^{15}N ion current is normally 10–20 nA on the sample with a beam spot circular and a radius of 2 mm. The average values of N_γ, Q, and c are given along with the stopping power, background noise and measuring time in table 4.1.

Because oxygen is a gas it can not form metallic bounds with the magnesium metal, instead ionic bounds are formed. This causes difficulty in determining the exact stopping power of MgO. The MgO stopping power (dE/dx) used here was taken from the program SRIM where the stopping power for the electrons and the nucleus were added together and the density of the film was taken as 3.581 g/cm^3 (Shackelford and Alexander, 2001, p. 78). This resulted in stopping power 2538.6 eV/nm (25386 MeV/cm) for MgO. The density of the grown films was not known so it adds uncertainties to the stopping power value.

It is possible to calculate how far the ^{15}N beam can penetrate the sample. This is calculated according to (Rydén et al., 1989)

$$x = \frac{-E_{res} + E}{dE/dx} \tag{4.2}$$

	Calibration sample	Grown MgO samples				
		Sample 1	Sample 2	Sample 3	Sample 4	Sample 5
Q $[\frac{\text{Å}}{s}]$	10000	10000	10000	10000	10000	10000
$\frac{dE}{dx}$ $[\frac{\text{MeV}}{\text{cm}}]$	31978	25386	25386	25386	25386	25386
N_γ [counts]	774	19	26	33	12	74
B $[\frac{\text{counts}}{s}]$	4.49×10^{-2}	4.49×10^{-2}	4.49×10^{-2}	4.49×10^{-2}	4.49×10^{-2}	4.49×10^{-2}
Δt [s]	154	153–156	152–156	153–154	153–155	154–156
c $[\frac{\text{atoms}}{\text{cm}^3}]$	9.21×10^{24}	0.30×10^{21}	0.47×10^{21}	0.64×10^{21}	0.12×10^{21}	1.66×10^{21}

Table 4.1: The given and the average of the measured values for each sample used in formula 4.1 along with the calibration sample. Where dE/dx is the stopping power of the material, N_γ is the number of detected γ quanta detected, B is the background contribution per time unit and is mainly due to cosmic radiation, Δt is the measuring time, Q is the ^{15}N dose given to the sample during the measuring time. The calibration sample (TaH$_{0.47}$) is denoted with subscript c and the grown samples are denoted with subscript s in equation 4.1 (Rydén et al., 1989).

where E_{res} is the resonance energy (6.384 MeV) and E is the energy of the ^{15}N beam. However, it can be difficult to determine the exact penetration depth because of the uncertainty of the stopping power of MgO. Growth parameters for samples used in the NRRA measurements are shown in table 3.1. Figure 4.1 shows the [H]/[MgO] ratio for the five films as a function of beam energy. There the energy steps while penetrating the overlaying Cr$_x$Mo$_{1-x}$ film have been removed from the graph. Using equation (4.2) to calculate the penetration into the sample, we find that the point at 6.9 MeV in figure 4.1 is at approximately 1500 Å inside the grown MgO film.

To get a value for the hydrogen concentration of each sample the average of the data measured was used. The average hydrogen concentration of the samples as a function of hydrogen partial pressure is shown in figure 4.2. The absolute value for the hydrogen partial pressure can be found in table 3.1 and the average value of the hydrogen concentration can be found in table 4.1. The hydrogen concentration is high even when no hydrogen is added to the growth environment. It should be noted that there are 10^{23} atoms/cm^3 of MgO in the crystal and the hydrogen concentration
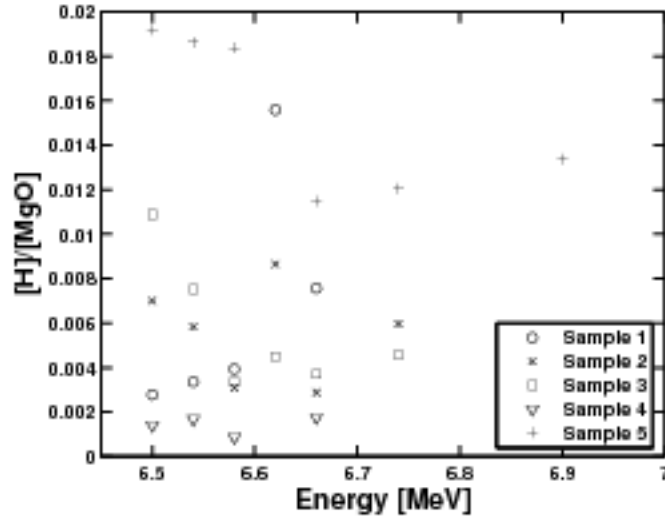
Figure 4.1: The ratio between [H] and [MgO] of the grown film versus energy of the ^{15}N beam. The energy of the ^{15}N beam is proportional to the penetration depth of the sample and can be calculated by equation (4.2)
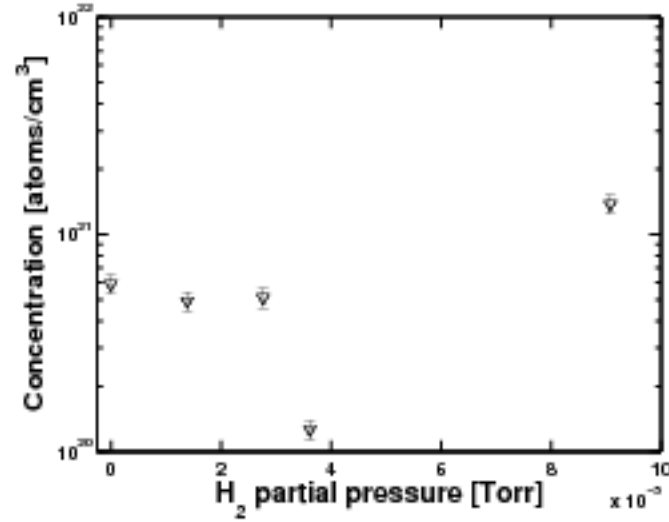

Figure 4.2: The average concentration of hydrogen [atoms/cm^3] in the MgO samples versus hydrogen partial pressure.

was measured to be of the order of 10^{21} atoms/cm^3. Figure 4.2 does not show increased hydrogen concentration as the hydrogen partial pressure is increased. This could indicate that even though the base pressure in the growth chamber is in the vicinity of 1×10^{-8} Torr the sample will be saturated with hydrogen. Other possible source for hydrogen are impurities in the target. Even though the target is 99.95 % pure magnesium metal, hydrogen can be at grain boundaries of the target material. This would possibly be a sufficient source of hydrogen to saturate the grown MgO film.

Equation (3.1) is useful to estimate the time it takes to grow one monolayer of impurities. Making the assumption that the base pressure is only hydrogen (for simplicity, the base pressure is mainly caused by water) we can say that the hydrogen pressure (p in equation (3.1)) in the chamber is in the vicinity of 3.0×10^{-8} Torr, (4×10^{-6} Pa). The molecular weight is M = 2 g/mol, the molecular diameter of hydrogen is around 2.34 Å which gives the number of atoms per unit area N_s = 1.82×10^{15} cm^{-2}, and the capacitors were grown at a temperature of T = 573 K. Based on these values, it takes approximately 59 s to grow one monolayer of hydrogen impurities, while the time it takes to grow 3000 Å of MgO is 1 hour and 51 minutes.

The uncertainty in the NRRA measurements is related to the counts of the detected γ particles along with the uncertainty of the stopping power in MgO. Because of low γ counts in the measurements, the uncertainty in the stopping power of MgO is dominating and is estimated to be around 10 %.

4.2 X–ray diffraction

To explore the structural properties of the MgO films X–ray diffraction (XRD) study was performed on a series of samples. For the XRD scan, samples were produced as described in section 3.5 and their growth parameters are shown in table 3.2. As can be seen in the XRD scans in figure 4.3 there are two peaks appearing for all of the grown thin films. The first peak shown in figure 4.3 (a) is around $43°$ and
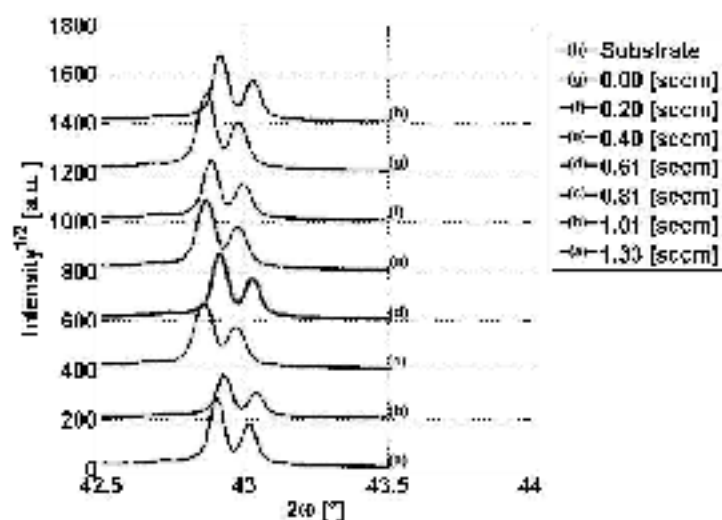
(a)
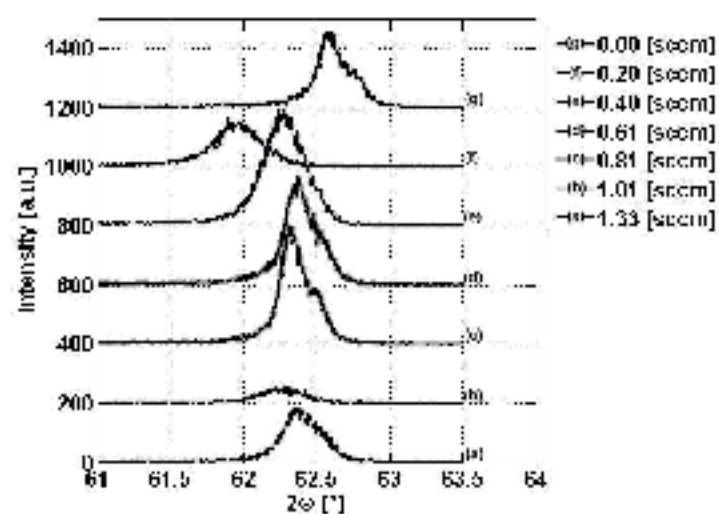
(b)

Figure 4.3: The XRD scan of the grown samples. As seen in figure (a) there is a peak around 43° which corresponds to the (2 0 0) orientation. The two peaks seen in this figure are due to two different wavelengths from the Cu anode in the X–ray device. In figure (b) another peak is seen between 62° and 63°. This peak is due to (2 2 0) orientation of the grown film.

corresponds to the (2 0 0) crystal plane, which is the same crystal plane as the MgO substrate. As can be seen there are two peaks around $43°$ which correspond to two different wavelengths, 1.5406 and 1.5444 Å, from the Cu anode in the X–ray device used for the XRD scan. The other peak shown in figure 4.3 (b) appears between $62°$ and $63°$ and corresponds to the (2 2 0) crystal plane of the crystal.

Cheng et al. (2002) and Zheng et al. (2006) have studied the growth orientation of MgO films, prepared by pulsed mid–frequency magnetron sputtering from a Mg target and cathodic–vacuum–arc ion deposition, respectively. Cheng et al. (2002) reported that the film orientation was dependent on the growth mode of the films. When growing MgO film on highly conducting n–type (2 0 0) Si substrate. They grew (2 0 0) oriented films in metal mode, but when the growth was in compound mode both (2 0 0) and (2 2 0) orientations were observed. Zheng et al. (2006) prepared MgO films on glass and Si substrates. They showed that the growth orientation was preferred to be (2 0 0) for high oxygen flow rate but (2 2 0) at relatively low oxygen flow rate.

By looking at figure 4.3, no effects of different hydrogen partial pressure in the growth chamber, while growing the films, on the orientation of the MgO films is observed. Which is in agreement with the results found by Aboelfotoh et al. (1977).

4.3 Electrical properties of thin film MgO

The capacitors made for the electrical measurements were grown at a different temperature than the samples made for the NRRA. Between the growth of the samples used for the NRRA measurement and the capacitors, targets were changed in the sputtering chamber. After the targets had been changed the best film growth was determined with X–ray scans as before. The best films, i.e. when the fringes from the XRR scan were visible at relatively high angles, were grown at 300 $°C$ compared to 500 $°C$ for the NRRA measurements. The XRR scan for the films grown at 500 $°C$ are shown in figure 4.4 and MgO film grown at $300°C$ is shown in figure 4.5. The change of targets resulted also in different growth rate than
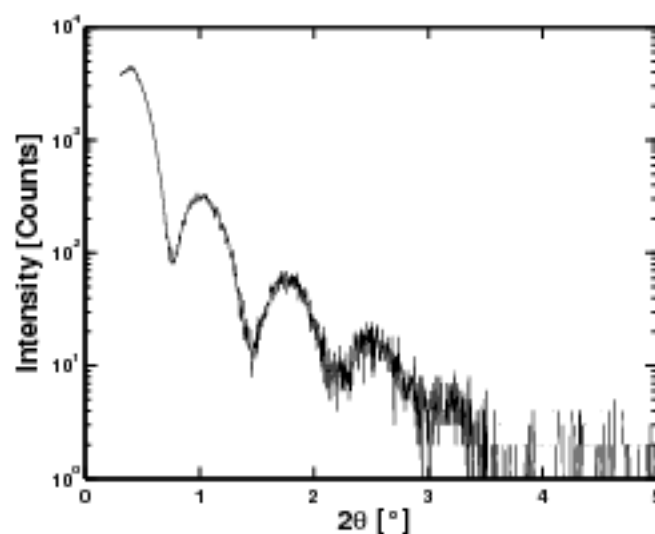
Figure 4.4: XRR–scan for a MgO film grown at 500°C. Fringes can be seen at relatively high angles witch indicate smooth surface.
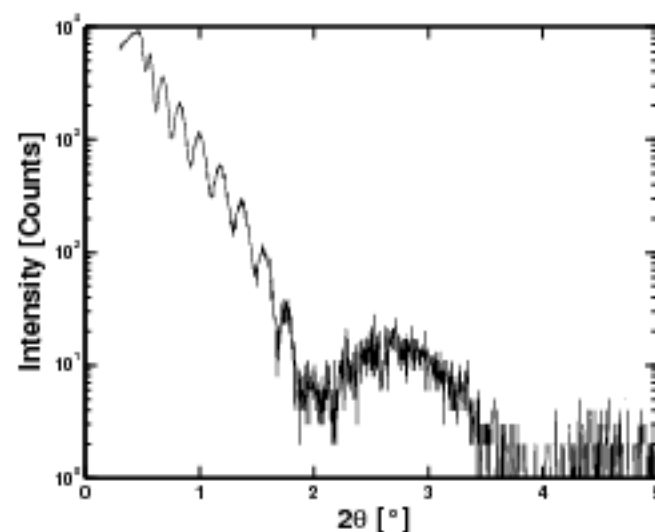

Figure 4.5: XRR–scan for a MgO film grown at 300°C. Fringes at relatively high angles indicate smooth surface.

before. The difference in temperature and growth rate are expected to affect the hydrogen concentration in the samples (Aboelfotoh et al., 1977). However, the NRRA measurements show that by increasing the hydrogen partial pressure in the growth environment does not results in higher hydrogen concentration in the grown samples.

The structure of the capacitors grown for the electrical measurement can be seen in figure 4.6. The edges, seen in that figure, are ideal spots for defects in the
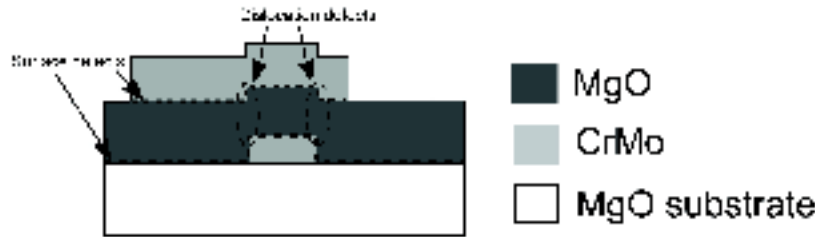
Figure 4.6: The structure of the capacitor can lead to defects in the MgO film such as surface and dislocation defects.

structure of the grown capacitors, such as surface and dislocation defects, and can explain different behavior between capacitors. On each substrate, six capacitors were grown as shown in figure 4.7, where the contacts 1 and 2 are contacts to the underlying Cr_xMo_{1-x} layer and contacts 3 to 8 are contacts to the overlaying Cr_xMo_{1-x} layer.

The capacitors, grown under different hydrogen partial pressure, were all measured. Their DC resistance at room temperature, as a function of hydrogen flow into the chamber, are shown in figure 4.8. Furthermore, the location of the capacitors on the sample is shown. As can be seen from the figure, the resistance of the capacitors changes several orders of magnitude for the samples with same amount of hydrogen flow into the chamber and no specific trend can be seen between the capacitors. It should be noted that the resistance at room temperature varies several orders of magnitude even between capacitors on the same substrate. There is also no obvious
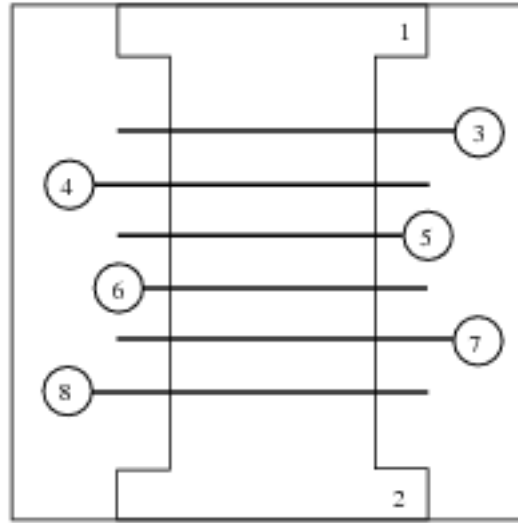
Figure 4.7: The layout of capacitors on the substrate. Contacts 1 and 2 are contacts to the underlying Cr_xMo_{1-x} layer and contacts 3 to 8 are contacts to the overlaying Cr_xMo_{1-x} film.
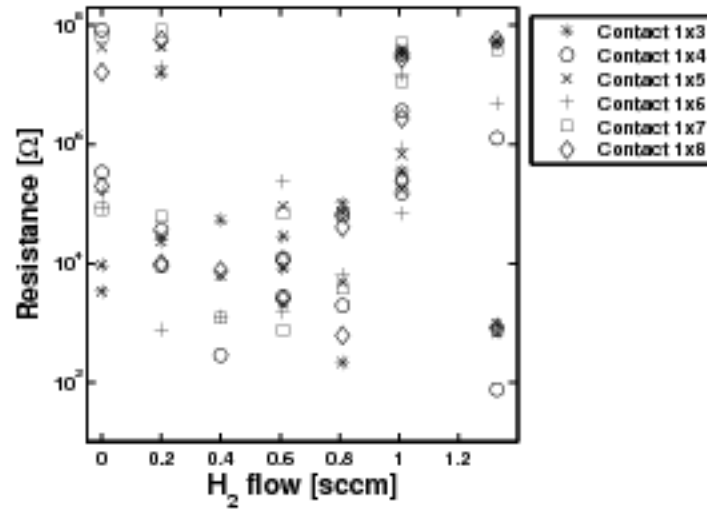

Figure 4.8: Electrical DC resistance at room temperature of the capacitors as a function of hydrogen flow into the chamber.

correlation between the resistance of the capacitors with regards to their location in the growing environment (different locations on the substrate), which could indicate nonuniformity in the plasma densities. This however was not expected, because of small size of the samples, and the relatively large distance between the sample and the target.

A likely reason which could possibly explain the variation in the resistance of the capacitors is their size. In figure 4.9 a sample of the grown capacitors is shown. As
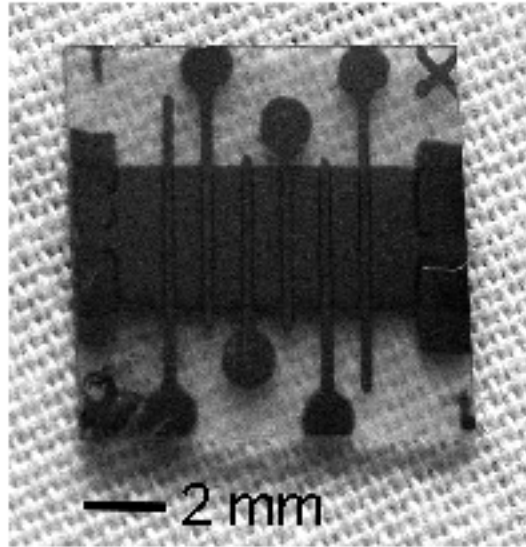
Figure 4.9: Figure of the grown capacitors.

can be seen from this figure the effective size (surface area) of the grown capacitors is large. Their effective size is $((16 \pm 8)) \times 10^{-3}$ cm^2. The large size of the surface area increases the probability of defects in the grown film. These defects can then be the cause of conduction in the grown MgO thin films.

The variation in the resistance does not indicate any effects from increasing hydrogen partial pressure in the growth environment. There is no correlation between the electrical resistance of the capacitors and the hydrogen partial pressure in the chamber.

The grown capacitors were modeled using the equivalent circuit shown in figure

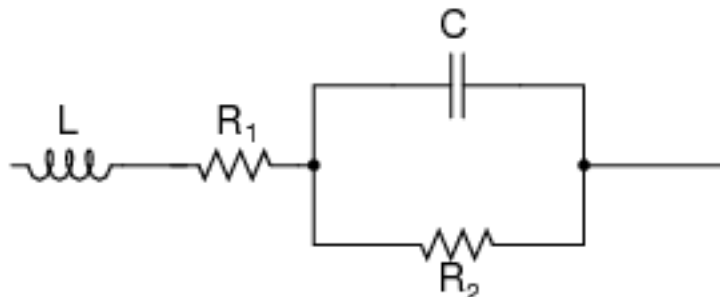4.10, where C and R_2 are the ideal capacitor and the leakage resistance of the capac-

Figure 4.10: Equivalent circuit of a capacitor and cables. An ideal capacitor (C) is connect parallel to a leakage resistance (R_2) which is connected in series to a inductance (L) and a resistance (R_1) of the cables and connections.

itors respectively. L and R_1 are then the inductance and resistance in connections and cables of the circuit used for the measurements.

4.4 Admittance spectroscopy

Here we discuss the admittance spectroscopy measurements of capacitors grown at various hydrogen partial pressures. A total of 11 capacitors were investigated over frequency range from 30 Hz to 1 MHz and by cooling them down to 78 K and heating them up to 400 K in steps. The layout of the capacitors on the substrate, which contained six capacitors on each substrate, can be seen in figure 4.7.

Two of the capacitors (capacitors 1 and 2) with high resistance are plotted in figure 4.11, where the amplitude of their admittance is plotted as a function of frequency. Information on their growth parameters is shown in table 4.2. The admittance for these two capacitors show very similar frequency response. There is very little variation in the admittances for different temperatures but some difference can be seen at the highest frequencies. The DC resistivity of the two capacitors at room temperature was 7×10^{10} Ωcm and 9×10^{10} Ωcm, respectively, which is one order of magnitude lower than reported by Soto et al. (1997).
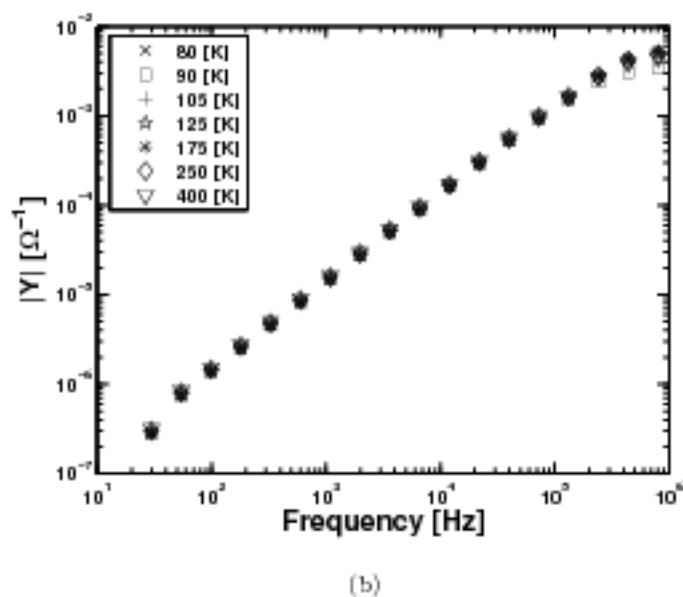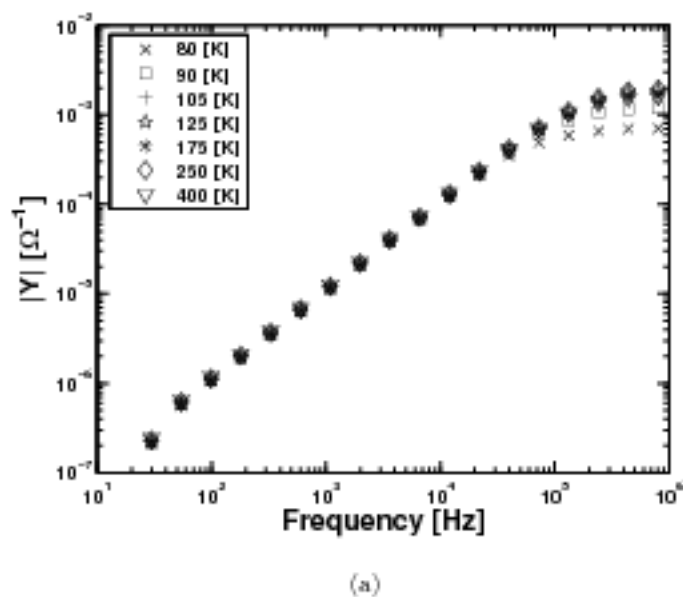
(a)

(b)

Figure 4.11: Admittance versus frequency at various temperatures for (a) Capacitor 1 grown with 0.00 sccm H_2 flow into the chamber, and (b) Capacitor 2 grown with 1.33 sccm H_2 flow into the chamber.

	Capacitor 1	Capacitor 2
DC Resistance $[\Omega]$	4.28×10^7	5.49×10^7
Resistivity, ρ $[\Omega$ cm$]$	$(7 \pm 4) \times 10^{10}$	$(9 \pm 5) \times 10^{10}$
Capacitance [nF]	1.79	2.32
Base press. [Torr]	4.79×10^{-9}	1.32×10^{-8}
Growth press. [Torr]	2.78×10^{-5}	2.71×10^{-5}
H_2 flow [sccm]	0.00	1.33
H_2 part. press. [Torr]	0.00	6.11×10^{-5}
O_2 part. press. [Torr]	8.53×10^{-5}	5.77×10^{-5}

Table 4.2: The growth parameters for the capacitors with high resistance at room temperature (capacitors 1 and 2).

It is interesting that these two highly resistive samples were grown on one hand with no additional hydrogen flow and on the other hand with highest flow applied to the chamber. As can be seen in figure 4.11 there is no thermal activation of conductivity in the temperature range 80 K to 400 K. The s parameter for capacitors 1 and 2, i.e. the slope of the curves in figure 4.11, is plotted in figure 4.12 as a function of temperature. The s parameter does not decrease with increasing temperature. According to the discussion in section 2.3 the slope of the curve and its temperature dependance tells if there is a hopping conduction in the dielectric. As figure 4.12 demonstrates there is no or very little variation in the s parameter. It stays very close to 1 and does not decrease with increased temperatures which indicate no correlated barrier hopping conduction in the MgO thin film.

To find the capacitance of the capacitors, the frequency response of the capacitors was found and compared to the equivalent circuit of a capacitor. The equivalent circuit used is shown in figure 4.10. This resulted in capacitance of the order of 10^{-9} F as can be seen in table 4.2 for capacitors 1 and 2, in table 4.3 for capacitors 3 to 8, and in table 4.4 for capacitors 9 to 11. Singh and Pratap (1982) reported on capacitors with capacitance of the order of 10^{-9} F when they studied Mg/MgO/Al capacitors with 40–200 Å thick MgO films.
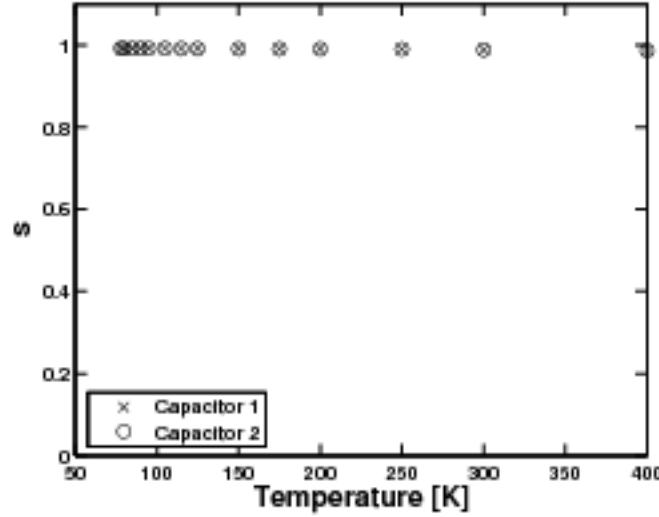
Figure 4.12: The *s* parameter versus temperature for capacitors 1 and 2. The *s* parameter does not decrease with temperature.

Another set of capacitors with similar resistance (approximately $10^5 \, \Omega$) at room temperature were measured as before in a cryostat in the same frequency and temperature interval. When the hydrogen flow was held 1.33 sccm no grown capacitor had resistance close to $10^5 \, \Omega$, either the capacitors had much lower resistance or higher than $10^6 \, \Omega$. Therefore, only capacitors grown with 0 to 1.01 sccm hydrogen flow into the chamber where measured (capacitors 3 to 8). The data for these capacitors and the growth parameters are listed in table 4.3.

Figure 4.13 shows the amplitude of the admittance versus frequency for capacitor 3 and capacitor 8. Capacitor 3 was grown with no additional hydrogen into the chamber and capacitor 8 was grown with 1.01 sccm of hydrogen flow into the chamber. These two capacitors show very similar behavior at all frequencies. Both have similar thermal activation of the conductivity at low frequencies but capacitor 8 has more variation of the conductivity at higher frequencies, with the lowest admittance measured at 105 K at high frequencies.

In figure 4.14 the *s* parameter for capacitors 3 to 8, are plotted as a function

	Capacitor 3	Capacitor 4	Capacitor 5
DC Resistance $[\Omega]$	8.16×10^4	6.07×10^4	5.41×10^4
Resistivity, ρ $[\Omega \ cm]$	$(1.3 \pm 0.7) \times 10^8$	$(10 \pm 5) \times 10^7$	$(9 \pm 5) \times 10^7$
Capacitance $[nF]$	2.57	2.94	2.87
Base press. $[Torr]$	5.18×10^{-8}	1.34×10^{-8}	9.53×10^{-9}
Growth press. $[Torr]$	2.75×10^{-5}	2.70×10^{-5}	2.75×10^{-5}
H_2 flow $[sccm]$	0.00	0.20	0.40
H_2 part. press. $[Torr]$	0.00	1.33×10^{-5}	2.69×10^{-5}
O_2 part. press. $[Torr]$	7.37×10^{-5}	5.91×10^{-5}	6.00×10^{-5}
	Capacitor 6	Capacitor 7	Capacitor 8
DC Resistance $[\Omega]$	2.40×10^5	7.04×10^4	6.88×10^4
Resistivity, ρ $[\Omega \ cm]$	$(4 \pm 2) \times 10^8$	$(1.1 \pm 0.6) \times 10^8$	$(1.1 \pm 0.6) \times 10^8$
Capacitance $[nF]$	3.26	2.23	2.73
Base press. $[Torr]$	1.52×10^{-8}	4.47×10^{-9}	3.88×10^{-9}
Growth press. $[Torr]$	2.78×10^{-5}	2.73×10^{-5}	2.71×10^{-5}
H_2 flow $[sccm]$	0.81	0.81	1.01
H_2 part. press. $[Torr]$	4.05×10^{-5}	5.29×10^{-5}	6.52×10^{-5}
O_2 part. press. $[Torr]$	6.02×10^{-5}	5.89×10^{-5}	5.81×10^{-5}

Table 4.3: The growth parameters for capacitors 3 to 8. The resistance was measured at room temperature.

of temperature. As that plot demonstrate there is very little variation in the s parameter. This is a similar behavior as shown for capacitors 1 and 2 (figure 4.12). The difference between capacitors 3 to 8 and capacitors 1 and 2 is the behavior at the lower frequencies. There capacitors 1 and 2 do not show any sign of thermal activation but for capacitors 3 to 8 thermal activation of the conductivity is observed.

The admittance curves as a function of frequency for capacitors 5 and 7 are shown in figure 4.15 (a) and (b) respectively. Capacitors 5 and 7 were grown while 0.4 and 0.81 sccm hydrogen flow was introduced into the chamber respectively. There is clearly a thermal activation of the conductivity in the low frequency regime.
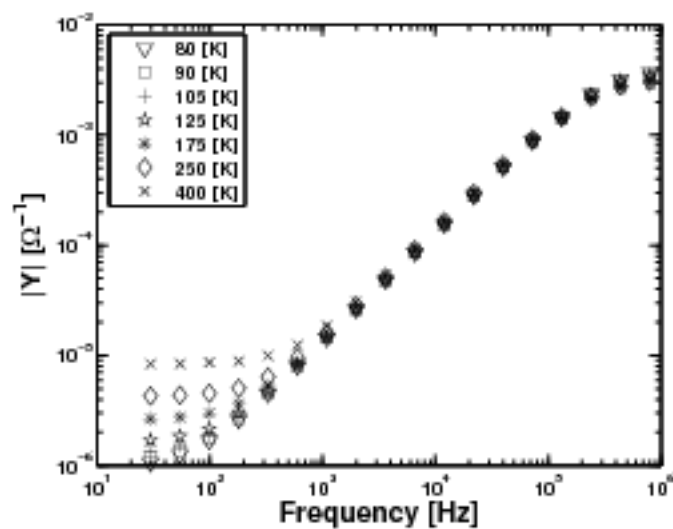
(a)
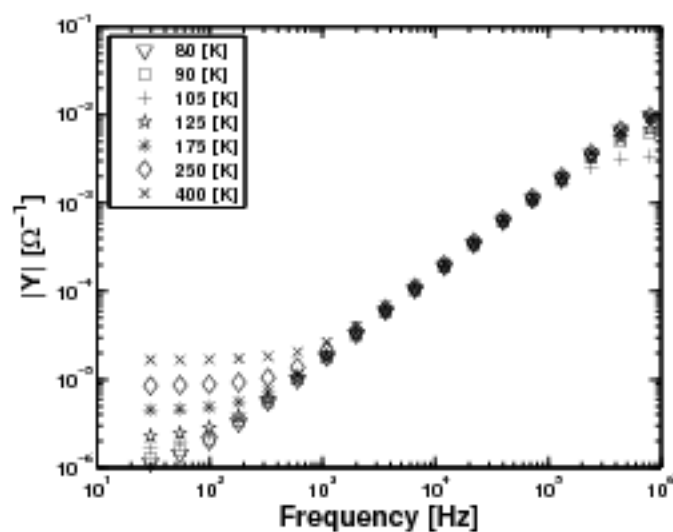
(b)

Figure 4.13: Admittance as a function of frequency at different temperatures for capacitors grown with (a) 0.00 sccm (capacitor 3) and (b) 1.01 sccm (capacitor 8) hydrogen flow into the chamber.

It is clear that the admittance does not change as much for capacitor 7 as it does for capacitor 5 at the lower frequencies. The activation energy observed in capacitors
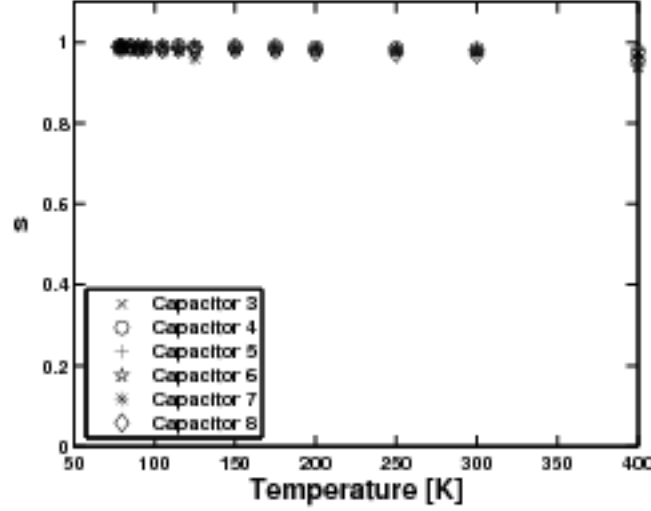
Figure 4.14: The s parameter of capacitors grown with different hydrogen flow into the chamber versus temperature. The resistance for all of these capacitors at room temperature was close to 10^5 Ω. The s parameters is close to 1 and does not decrease much with temperature which indicates no correlated barrier hopping conduction in the capacitors.

3, 5, 7, and 8 is of the order of 20–30 meV, compared to few hundred meV at little higher temperatures (room temperature to 800 K) found by Lempicki (1953) in bulk MgO. Capacitor 7 has larger variation in the admittance at higher frequencies than other capacitors measured. When capacitor 7 was measured at 125 K it resulted in the lowest admittance at the high frequencies and the second lowest admittance resulted at 90 K. The capacitor had similar admittance at other temperatures in the high frequency region.

However, some of the measured capacitors show a different behavior. When capacitors with a low resistance at room temperature were measured at different temperatures the slope of the curve changed with increasing temperature. In figure 4.16 comparison of two capacitors (capacitors 9 and 10) grown at different hydrogen partial pressure is shown. For the capacitor grown at higher hydrogen partial pressure (capacitor 10), as can be seen in figure 4.16 (b) the slope of the curve changes as
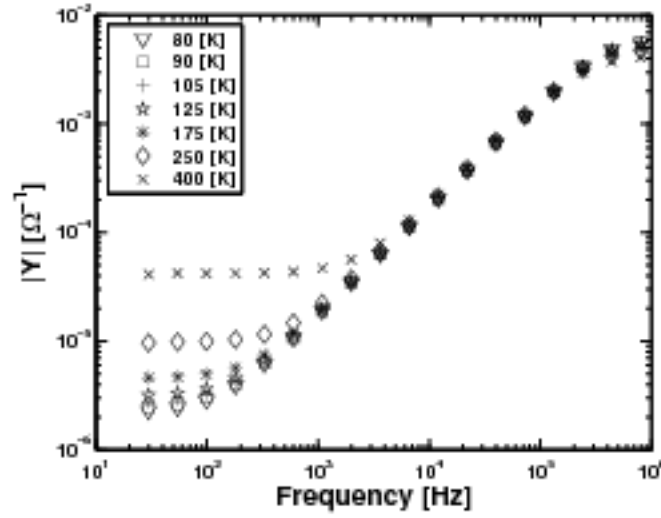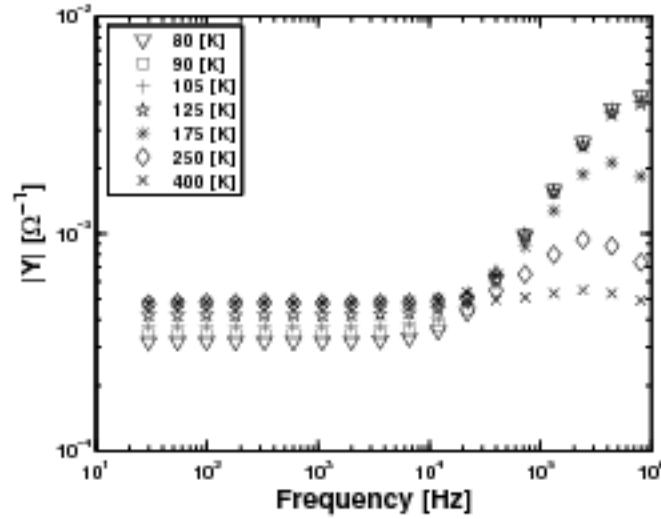
(a)
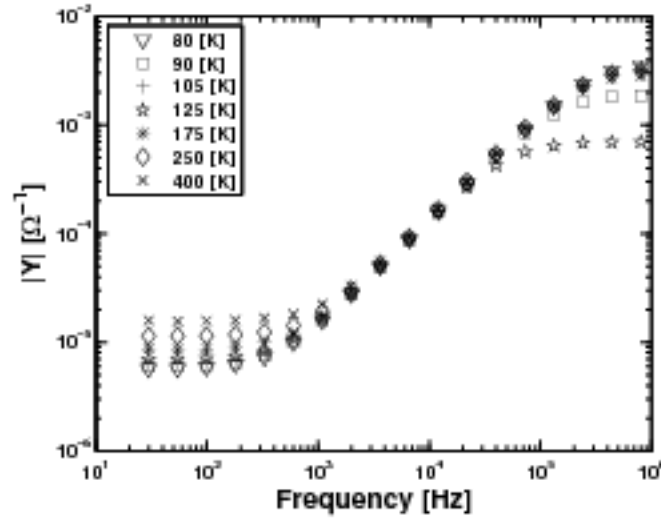
(b)

Figure 4.15: Admittance versus frequency at various temperatures for (a) capacitor 5 and (b) capacitor 7. Both capacitors show thermal activation of the conductivity at low temperatures.

the temperature is increased. This behavior is not as obvious for capacitor 9 shown in figure 4.16 (a). This conduction mechanism is not metallic like conduction as
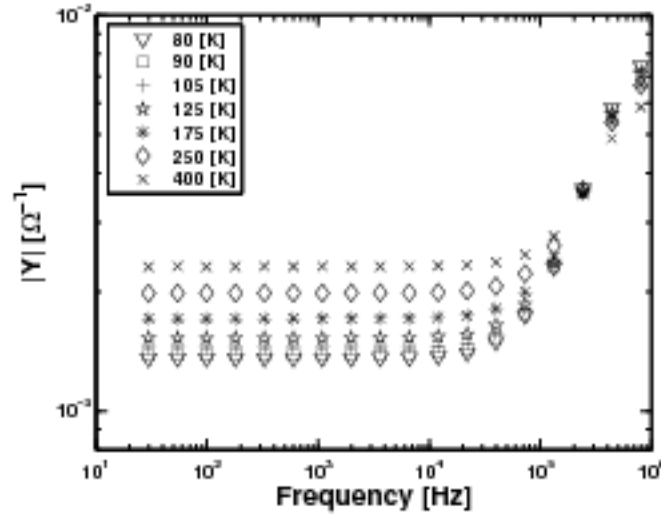
(a)

(b)

Figure 4.16: The admittance versus frequency at various temperatures for (a) capacitor 9 grown with 0.4 sccm hydrogen flow into the chamber and (b) capacitor 10 grown with 1.33 sccm hydrogen flow into the chamber. As can be seen clearly for capacitor 10 the slope of the plot is decreasing with higher temperatures which indicate hopping conduction in the capacitors.

the admittance decreases with decreasing temperature. The growth parameters for three capacitors that show this behavior are shown in table 4.4.

	Capacitor 9	Capacitor 10	Capacitor 11
DC Resistance [Ω]	284	755	75
Resistivity, ρ [Ω cm]	$(5 \pm 2) \times 10^5$	$(1.2 \pm 0.7) \times 10^6$	$(1.2 \pm 0.7) \times 10^5$
Capacitance [nF]	2.95	2.38	3.96
Base press. [Torr]	9.53×10^{-9}	3.75×10^{-9}	3.75×10^{-9}
Growth press. [Torr]	2.75×10^{-5}	2.95×10^{-5}	2.95×10^{-5}
H_2 flow [sccm]	0.40	1.33	1.33
H_2 part. press. [Torr]	2.69×10^{-5}	9.30×10^{-5}	9.30×10^{-5}
O_2 part. press. [Torr]	6.00×10^{-5}	6.28×10^{-5}	6.28×10^{-5}

Table 4.4: The growth parameters for the capacitors (capacitors 9 to 11) which show correlated barrier hopping, i.e. decreasing s parameter with higher temperatures. Capacitors 10 and 11 are both grown on the same sample and capacitor 9 is grown on the same sample as capacitor 5. The resistance was measured at room temperature.

Capacitors 10 and 11 are both grown on the same substrate and therefore both grown at 1.33 sccm hydrogen flow into the chamber. However, capacitor 9 is grown at 0.40 sccm hydrogen flow. Capacitor 9 is grown on the same substrate as capacitor 5 and is beside it on the substrate (contacts 1×4 and 1×3 respectively). However, capacitor 5 does not show the same behavior in the s parameter as capacitor 9.

The s parameter for capacitors 9, 10, and 11 are shown in figure 4.17. It is noted that the s parameter drops with increasing temperature for all capacitors. As mentioned in section 2.3 this behavior indicates correlated barrier hopping conduction in the samples. It is interesting that the s parameters for capacitors 10 and 11 show different behavior with temperature even though they are grown on the same substrate and therefore in the same growth environment and at the same hydrogen flow. Because only few of the capacitors show this behavior and the different behavior in the s parameter for capacitors 10 and 11, which are grown with the same hydrogen flow, it is more likely that this behavior is not hydrogen related
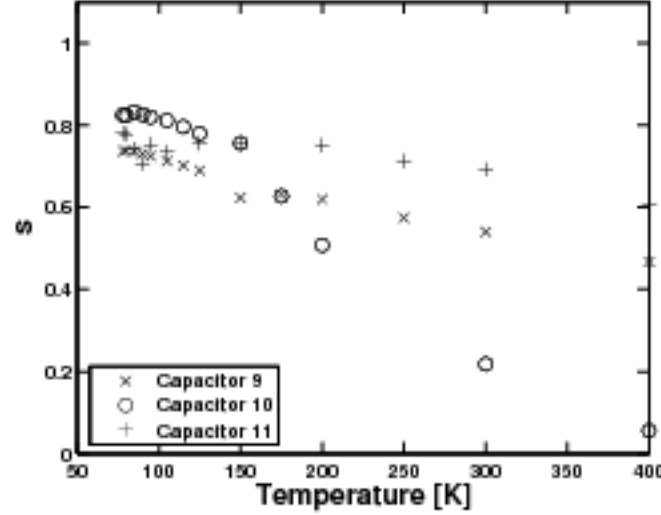
Figure 4.17: The s parameter versus temperature for capacitors 9, 10 and 11. The s parameter for these capacitors decreases with temperature which indicates correlated barrier hopping conduction.

defects in the MgO film, rather it has to do with defects at the interfaces between the Cr_xMo_{1-x} and the MgO film.

The temperature dependence of s has been reported by Deroide et al. (1995) where they looked at transport properties in polycrystalline MgO. For their studies they used samples in powder form of purity higher than 99.99 % and with grain size less than 200 μm. Their measurements were made in the temperature range from 518 to 860 °C and showed s decreasing with increasing temperature.

The measured phase of the capacitors 1 to 11 are shown in figures 4.18, 4.19, and 4.20. The phase was measured at room temperature and four point probe technique was used. The difference in the phase between these figures is obvious. Capacitors 1 and 2 (figure 4.18) show expected behavior of a capacitor starting at -90° and then increases at roughly 10 kHz due to inductance in the cables. The phase measured for capacitors 3 to 8 (shown in figure 4.19) starts at 0° and then decreases to a minimum between -80° and -90° at roughly 10 kHz. After 10 kHz the phase increases because
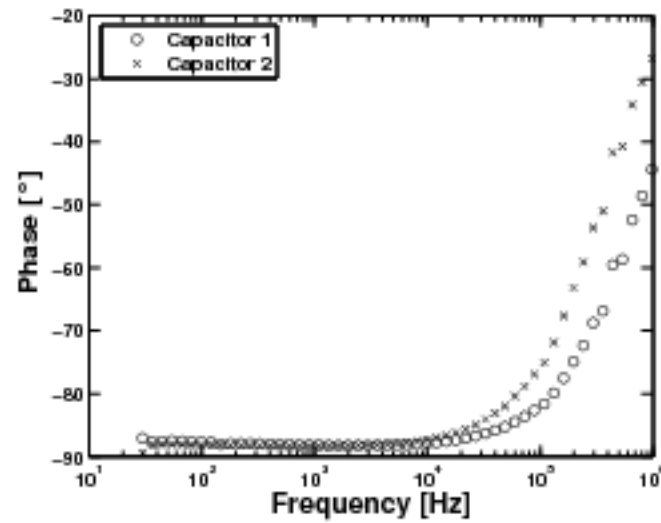
Figure 4.18: The admittance phase for capacitors 1 and 2 versus frequency. The phase starts at 90°. At about 10 kHz the phase starts to deviate from -90° due to inductance in the cables.
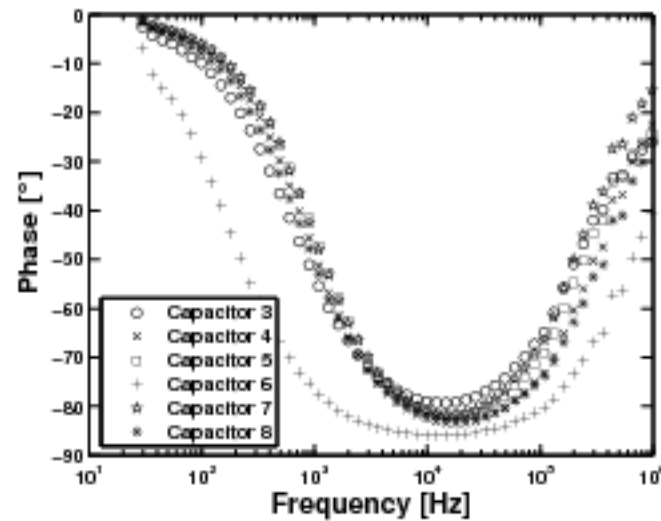

Figure 4.19: The Admittance phase for capacitors 3 to 8 versus frequency. The phase starts at 0° and decreases and is between -80 and -90° at frequencies around 10 kHz and then increases again due to inductance in the cables.
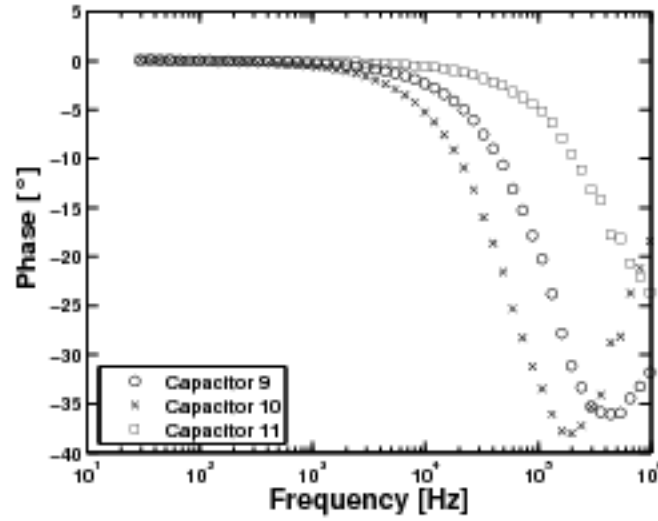
Figure 4.20: The admittance phase for capacitors 9 to 11 versus frequency. The phase stays at $0°$ in the frequency range 1–10 kHz when it starts to decrease.

of inductance in the cables. The phase of capacitors 9 to 11 (shown in figure 4.20) start as capacitors 3 to 8 at $0°$ and decreases for frequencies in the range of 1–10 kHz and decreases until the inductance of the cables compensate for the capacitance at 100 kHz. The behavior of the capacitors 3 to 11, i.e. the phase starting at $0°$, can be explained by looking at the capacitor equivalent circuit in figure 4.10. At low frequencies the ideal capacitor (C in figure 4.10) has a very high resistance but with increasing frequency the resistance of the capacitor decreases at the same time the leakage resistance is constant. At low frequencies the leakage resistance (R_2 in figure 4.10) is dominating. An ideal resistance does not effect the phase of the capacitor and therefore it starts at $0°$ until the frequency is high enough so the resistance of the ideal capacitor has decreased and is comparable or lower than the leakage resistance. At that point the phase of the capacitors is affected.

4.5 Aging

The admittance of some of the capacitors was seriously affected when measured at room temperature one month after they were grown. Capacitor 6 was measured 10^{-5} Ω^{-1} just after the growth but was measured 10^{-2} Ω^{-1} one month later after being stored at room temperature for one month in the atmosphere. To see if annealing
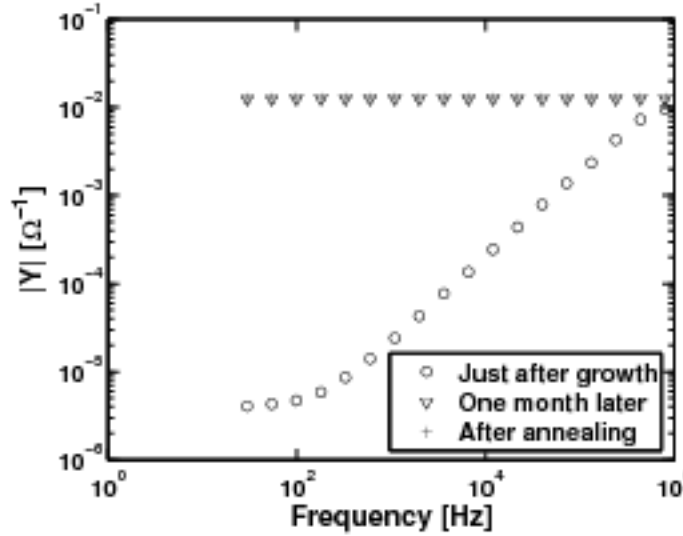

Figure 4.21: The admittance versus frequency of Capacitor 6 measured right after growth, one month after growth, and after annealing in oxygen environment at 500 °C for one hour. The capacitor was stored in ambient air at room temperature.

affected the admittance of the capacitor it was annealed at 723 K with high oxygen partial pressure for one hour. The heat was increased from room temperature by 30 °C/min. The annealing temperature was chosen according to results from Freund et al. (1984). Their results showed maximum H_2 release from MgO crystal at temperatures between 600–800 K. Furthermore, Aboelfotoh et al. (1977) showed that annealing MgO crystal at 723 K for 30 minutes in dry nitrogen most of the hydrogen groups in the films were removed. While annealing the capacitor 30 sccm of oxygen was introduced into to chamber. The base pressure in the chamber before annealing was 1.10×10^{-5} Torr and the pressure while annealing the sample was

1.60×10^{-3} Torr. In figure 4.21 the measured admittance is shown versus frequency just after growth, one month later, and after annealing in oxygen environment for one hour for capacitor 6. As shown in figure 4.21, annealing the capacitor at 500 K did not affect the admittance of the capacitor. The admittance was still in the order of 10^{-2} Ω^{-1}. The observed damage was permanent.

Chapter 5

Conclusions

Hydrogen is present in any growth environment. Therefore, it can be incorporated into grown films. The amount of impurities depends on growth temperature, partial pressure, hydrogen uptake of the films and film growth rate. In this study hydrogen was introduced into the growth chamber of a magnetron sputtering discharge to increase the hydrogen partial pressure during growth. The effects of hydrogen impurities on the thin film MgO electrical properties were then investigated. Measurements with nuclear resonance reaction analysis showed that the hydrogen content of the grown films did not depend on the hydrogen partial pressure in the growth chamber. The hydrogen partial pressure was in the range from 10^{-8} Torr to 10^{-6} Torr. This can possibly indicate hydrogen saturation in the MgO crystal because the hydrogen partial pressure was increased drastically between sample 1 and sample 2.

There is a significant variation in the resistance of the capacitors at room temperature, even for those grown at similar hydrogen partial pressure. However, there is no correlation between the hydrogen flow into the chamber and the resistance. Some of the capacitors have high electrical resistance with no thermal activation of the conductivity at low frequencies. Some of the capacitors show signs of correlated barrier hopping, some do not, and other capacitors show thermal activation of the conductivity at low frequencies. It is therefore reasonable to conclude that hydro-

gen does not have dominating effects on the insulating properties of the thin MgO films in the pressure range from 10^{-8} Torr to 10^{-5} Torr. This is in agreement with the calculations performed by Kiliç and Zunger (2002). The capacitors with very low resistance at room temperature, showed decreasing s parameter with increasing temperature. This is suggested to be due to correlated barrier hopping in the MgO film. The stability of some of the capacitors was also not as good as expected. The resistance decreased three orders of magnitude over a period of one month when stored in an atmospheric ambient at room temperature. Annealing in oxygen rich environment at 500 °C for one hour did not improve or affect the resistance in any way.

Two reasons can be considered causing the high variation in the DC resistance of the capacitors. First it has to be considered that the effective size (surface area) of the capacitors is large $((16 \pm 8) \times 10^{-3}$ cm$^2)$. When the size of the capacitor is large the probabilities of defects at the interfaces are increased. Another likely reason for this behavior is the ion bombardment of high-energy atoms and ions on the substrate as discussed in section 2.9. Because of these high-energy oxygen atoms and ions which are produced in the magnetron sputtering chamber, it is difficult to grow highly insulating films such as MgO in a magnetron sputtering system.

List of Tables

Bibliography

Aboelfotoh, M., K. Park, and W. Pliskin (1977). Infrared and high–energy electron diffraction analyses of electron–beam–evaporated MgO films. *Journal of Applied Physics 48*(7), 2910–2917.

Agustsson, J. S. (2005, June). Electrical characterization of MgO thin films grown by reactive magnetron sputtering. Master's thesis, University of Iceland, Reykjavik.

Berg, S., H.-O. Bloom, T. Larsson, and C. Nender (1987). Modeling of reactive sputtering of compound materials. *Journal of Vacuum Science and Technology A 5*(2), 202 – 207.

Berg, S. and T. Nyberg (2005). Fundamental understanding and modeling of reactive sputtering process. *Thin Solid Films 476*(2), 215 – 230.

Briere, M. (1993, February). *Hydrogen Incorporation and Radiation Induced Dynamics in Metal-Oxide-Silicon Structures. A Study using Nuclear Reaction Analysis.* Ph. D. thesis, Der Technischen Universität Berlin.

Chambers, S. A., Y. Gao, and Y. Liang (1995). The early stages of MgO epitaxy on lattice-matched $Cr_{0.7}Mo_{0.3}(001)$. *Surface Science 339*(3), 297 – 309.

Chapin, J. S. (January 1974). The planar magnetron. *Research/Develoment*, 37 – 40.

Cheng, Y., H. Kupfer, U. Krause, T. Kopte, C. Peters, and F. Richter (2004). Influence of O_2 flow rate on the structural properties of MgO films deposited by dual magnetron sputtering. *Surface & Coatings Technology 177*, 784 – 788.

Cheng, Y. H., H. Kupfer, F. Richter, and A. M. Paraian (2002). Deposition of MgO films by pulsed mid-frequency magnetron sputtering. *Applied Surface Science 200*(1-4), 117–124.

65

Choi, Y. W. and J. Kim (2004). Reactive sputtering of magnesium oxide thin film for plasma display panel applications. *Thin Solid Films 460*, 295 – 299.

Cullity, B. D. (1978). *Elements of X-Ray Diffraction, 2nd ed.* London: Addison-Wesley.

de Walle, C. G. V. (2000). Hydrogen as a cause of doping in zinc oxide. *Physical Review Letters 85*(5), 1012–1015.

Deroide, B., B. Bertheville, and J. Zanchetta (1995). Transport properties of polycrystalline samples of calcium and magnesium oxides. experimental and theoretical approaches. *Journal of Physics and Chemistry of Solids 56*(7), 989–994.

Duriez, C., C. Chapon, C. R. Henry, and J. M. Rickard (1990). Structural characterization of MgO(100) surfaces. *Surface Science 230*(1–3), 123–136.

Elliott, S. R. (1978). Temperature dependence of a.c. conductivity of chalcogenide glasses. *Philosophical Magazine B 37*(5), 553–560.

Elliott, S. R. (1987). A.c conduction in amorphous chalcogenide and pnictide semiconductors. *Advances in Physics 36*(2), 135–218.

Engkvist, O. and A. J. Stone (1999). Adsorption of water on the MgO(001) surface. *Surface Science 437*(1-2), 239–248.

Fan, W., P. Markworth, T. Marks, and R. Chang (2001). Growth of atomically flat homoepitaxial mangesium oxide thin films by metal-organic chemical vapor deposition. *Materials Chemistry and Physics 70*(2), 191 – 196.

Freund, F., B. King, R. Knobel, and H. Katherein (1984). Low atomic number impurity atoms in magnesium oxide: Hydrogen and carbon. *Advances in Ceramics 10*, 119–138.

Freund, F., R. Knobel, H. Kathrein, and H. Wengeler (1984). Pre-irradiation defects in "pure" MgO associated with hydrogen carbon and peroxy configurations. *Nuclear Instruments and Methods in Physics Research B 229*(2–3), 223–234.

Ghosh, A. (1990). Frequency-dependent conductivity in bismuth-vanadate glassy semiconductors. *Physical Review B 41*(3), 1479–1488.

Gylfason, K. B., A. S. Ingason, J. S. Agustsson, S. Olafsson, K. Johnsen, and J. T. Gudmundsson (2006). In-situ resistivity measurements during growth of ultra-thin $Cr_{0.7}Mo_{0.3}$. *Thin Solid Films 515*(2), 583–586.

Hamerich, A., R. Wunderlich, and J. Müller (1994). Modeling of deposition and resputtering rate profiles in planar face to face sputtering systems. *Journal of Vacuum Science and Technology A 12*(5), 2873–2878.

Holý, V., U. Pietsch, and T. Baumback (1999). *High-Resolution X-Ray Scattering from Thin Films and Multilayers*. Berlin: Springer.

Hsu, W.-Y. and R. Raj (1992). MgO epitaxial thin films on (100) GaAs as a substrate for the growth of oriented $PbTiO_3$. *Applied Physics Letters 60*(25), 3105 – 3107.

Ishibashi, S., Y. Higuchi, Y. Ota, and K. Nakamura (1990). Low resistivity indium–tin oxide transparent conductive films. II. Effect of sputtering voltage on electrical properties of films. *Journal of Vacuum Science and Technology A 8*(3), 1403–1406.

Jonscher, A. K. (1972). Frequency-dependence of conductivity in hopping systems. *Journal of Non-Crystalline Solids 8-10*, 293–315.

Kathrein, H. and F. Freund (1983). Electrical conductivity of magnesium oxides single crystal below 1200 K. *Journal of Physics and Chemistry of Solids 44*(3), 177–186.

Kelly, P. and R. Arnell (1999). Control of the structure and properties of aluminum oxide coatings deposited by pulsed magnetron sputtering. *Journal of Vacuum Science and Technology A 17*(3), 945 – 953.

Kelly, P. J., P. S. Henderson, R. D. Arnell, G. A. Roche, and D. Carter (2000). Reactive pulsed magnetron sputtering process for alumina films. *Journal of Vacuum Science and Technology A 18*(6), 2890 – 2896.

Kerber, G., J. Cooper, R. Morris, J. Spargo, and A. Toth (1989). NbN/MgO/NbN Josephson tunnel junctions fabricated on thin underlayers of MgO. *IEEE Transactions on Magnetics 25*(2), 1294 – 1296.

Kester, D. J. and R. Messier (1986). Predicting negative ion resputtering in thin films. *Journal of Vacuum Science and Technology A 4*(3), 496–499.

Kiliç, Ç. and A. Zunger (2002). n–type doping of oxides by hydrogen. *Applied Physics Letters 81*(1), 73 – 75.

Kingery, W., H. Bowen, and D. Uhlmann (1975). *Introduction to Ceramics* (2 ed.). New York: John Wiley & Sons.

Lal, K., S. K. Chattopadhyay, A. Meikap, S. Chatterjee, and M. Ghosh (2003). Frequency dependent conductivity of ZnO films prepared by r.f. sputtering technique. *Czechoslovak Journal of Physics 53*(3), 263 – 270.

Lanford, W. and M. Rand (1978). The hydrogen content of plasma-deposited silicon nitride. *Journal of Applied Physics 49*(4), 2473–2477.

Lanford, W., H. Trautvetter, J. Ziegler, and J. Keller (1976). New precision technique for measuring the concentration versus depth of hydrogen in solids. *Applied Physics Letters 28*(9), 566–568.

Lee, J. H., J. H. Eun, S. G. Kim, S. Y. Park, M. J. Lee, and H. J. Kim (2003). Hydration behavior of MgO single crystals and thin films. *Journal of Materials Research 18*(12), 2895–2903.

Lee, J. H., J. H. Eun, S. Y. Park, S. G. Kim, and H. J. Kim (2003). Hydration of r.f. magnetron sputtered MgO thin films for a protective layer in ac plasma display panel. *Thin Solid Films 435*(1–2), 95 – 101.

Lempicki, A. (1953). Electrical conductivity of MgO single crystal at high temperatures. *Physical Society – Proceedings 66*(400).

Lewis, T. and A. Wright (1968). The electrical conductivity of magnesium oxide at low temperatures. *British Journal of Applied Physics 1*(2), 441–447.

Lieberman, M. A. and A. J. Lichtenberg (1994). *Principles of Plasma Discharges and Materials Processing.* New York: John Wiley & Sons.

Matsuda, Y., M. Iwaya, Y. Koyama, M. Shinohara, and H. Fujiyama (2004). Effect of inductively-coupled plasma assist on the crystal orientation of magnesium oxide films produced by reactive sputtering. *Thin Solid Films 457*(1), 64 – 68.

Mejias, J. A., A. J. Berry, K. Refson, and D. G. Fraser (1999). The kinetics and mechanism of MgO dissolution. *Chemical Physics Letters 314*(5–6), 558–563.

Mitoff, S. (1961). Electronic and ionic conductivity in single crystals of MgO. *Journal of Chemical Physics 36*(5), 1383 – 1389.

Osburn, C. and R. Vest (1971). Electrical properties of single crystals, bicrystals, and polycrystals of MgO. *Journal of The American Ceramic Society 54*(9), 428 – 435.

Parkin, S. S. P., C. Kaiser, A. Panchula, P. M. Rice, B. Hughes, M. Samant, and S.-H. Yang (2004). Giant tunneling magnetoresistance at room temperature with MgO (100) tunnel barriers. *Nature Materials 3*(12), 862–867.

Pike, G. E. (1972). ac conductivity of scandium oxide and a new hopping model for conductivity. *Physical Review B 6*(4), 1572–1580.

Rakotomiraho, S., E. Charles, and A. Boyer (1986). Some physical properties of thin MgO films produced by reactive evaporation. *Journal of Materials Science 21*(6), 2124 – 2128.

Refson, K., R. Wogelius, D. Fraser, M. Payne, M. Lee, and V. Milman (1995). Water chemisorption and reconstruction of the MgO surface. *Physical Review B 52*(15), 10823 – 10826.

Rossnagel, S. M. and J. J. Cuomo (1988). Ion beam bombardment effects during film deposition. *Vacuum 38*(2), 73–81.

Rydén, J., B. Hjörvarsson, T. Ericsson, E. Karlsson, A. Krozer, and B. Kasemo (1989). Unusual kinetics of hydride formation in Mg–Pd sandwiches, studied by hydrogen profiling and quartz crystal microbalance measurement. *Journal of the Less-Common Metals 152*(2), 295 – 309.

Samson, S. and C. Fonstad (1973). Defect structure and electronic donor levels in stannic oxide crystals. *Journal of Applied Physics 44*(10), 4618–4621.

Schiller, S., K. Goedicke, J. Reschke, V. Kirchhoff, S. Schneider, and F. Milde (1993). Pulsed magnetron sputter technology. *Surface & Coatings Technology 61*(1–3), 331–337.

Schneider, J. M., A. Anders, B. Hjörvarsson, I. Petrov, K. Macák, U. Helmersson, and J.-E. Sundgren (1999). Hydrogen uptake in alumina thin films synthesized from an aluminum plasma stream in an oxygen ambient. *Applied Physics Letters 74*(2), 200–202.

Schneider, J. M., B. Hjörvarsson, X. Wang, and L. Hultman (1999). On the effect of hydrogen incorporation in strontium titanate layers grown by high vacuum magnetron sputtering. *Applied Physics Letters 75*(22), 3476–3478.

Selinder, T. I., G. Larsson, and U. Helmersson (1991). Resputtering effects on the stoichiometry of YBa$_2$Cu$_3$O$_x$ thin films. *Journal of Applied Physics 69*(1), 390–395.

Sellers, J. (1998). Asymmetric bipolar pulsed DC: The enabling technology for reactive PVD. *Surface & Coatings Technology 98*(1–3), 1245 – 1250.

Sempolinski, D., W. Kingery, and H. Tuller (1980). Electronic conductivity of single crystalline magnesium oxide. *Journal of The American Ceramic Society 63*, 669–675.

Shackelford, J. F. and W. Alexander (2001). *Materials science and engineering handbook* (Third ed.). CRC.

Shintani, Y., K. Nakanishi, T. Takawaki, and O. Tada (1975). Behaviours of high–energy electrons and neutral atoms in the sputtering of BaTiO$_3$. *Japanese Journal of Applied Physics 14*(12), 1875–1879.

Singh, A. and R. Pratap (1982). A.C. electrical breakdown in thin magnesium oxide films. *Thin Solid Films 87*(2), 147 – 150.

Smith, D. L. (1995). *Thin-Film Deposition, Principles and Practice*. New York: McGraw-Hill.

Soto, R., S. Mergui, and P. E. Schmidt (1997). Electrical and mechanical properties of MgO thin films on GaAs. *Thin Solid Films 308-309*, 611–614.

Sze, S. M. (2002). *Semiconductor Devices, Physics and Technology* (2nd ed.). New York: Wiley.

Tanaka, S., H. Nakanishi, T. Matsuura, K. Higaki, H. Itozaki, and S. Yazu (1991). Epitaxial growth of YBCO/MgO/YBCO structures. *IEEE Transactions on Magnetics 27*(11), 1607–1611.

Tominaga, K., Y. Sueyoshi, C. Munfei, and Y. Shintani (1993). Energetic O$^-$ ions and O atoms in planar magnetron sputtering of ZnO target. *Japanese Journal of Applied Physics 32*(9B), 4131–4135.

Tominaga, K., N. Ueshiba, Y. Shintani, and O. Tada (1981). High-energy neutral atoms in the sputtering of ZnO. *Japanese Journal of Applied Physics 20*(3), 519–526.

Vuoristo, P., T. Mantyla, P. Kettunen, and R. Lappalainen (1991). RBS analysis of sputter-deposited MgO films. *Vacuum 42*(15), 1001 – 1004.

Waits, R. K. (1978). Planar magnetron sputtering. *Journal of Vacuum Science and Technology 15*(2), 179 – 187.

Xiong, F., F. Rauch, C. Shi, Z. Zhou, P. Livi, and T. Tombrello (1987). Hydorgen depth profiling in solids: A comparison of several nuclear reaction techniques. *Nuclear Instruments and Methods in Physics Research B 27*(3), 432–441.

Yamano, K., L. Shimanoka, K. Takahashi, T. Usuki, Y. Yoshisato, and S. Nakano (1993). Fabrication and properties of $Nb/MgO/Bi_2Sr_2CaCu_2O_x$ tunnel junctions using crystalline and amorphous MgO films grown by the MBE method. *IEEE Transactions on Applied Superconductivity 3*(1), 2222 – 2225.

Yuasa, S., T. Nagahama, A. Fukushima, Y. Suzuki, and K. Ando (2004). Giant room-temperature magnetoresistance in single-crystal Fe/MgO/Fe magnetic tunnel junctions. *Nature Materials 3*(12), 868–871.

Zafar, S., C. Cabral, J. R. Amos, and A. Callegari (2002). A method for measuring barrier heights, metal work functions and fixed charge densities in metal/SiO_2/Si capacitors. *Applied Physics Letters 80*(25), 4858 – 4860.

Zafar, S., K. Conrad, Q. Liu, E. Irene, G. Hames, R. Kuehn, and J. Wortman (1995). Thickness and effective electron mass measurements for thin silicon dioxide films using tunneling current oscillations. *Applied Physics Letters 67*(7), 1031 – 1033.

Zafar, S., Q. Liu, and E. Irene (1994). Study of tunneling current oscillation dependence on SiO_2 thickness and Si roughness at the SiO_2/ Si interface. *Journal of Vacuum Science and Technology A 13*(1), 47 – 53.

Zheng, C., D. Zhu, D. Chen, Z. He, L. Wen, W. Cheung, and S. Wong (2006). Influence of O_2 flow rate on structure and properties of MgO_x films prepared by cathodic-vacuum-arc ion deposition system. *IEEE Transactions on Plasma Science 34*(4), 1099–1104.

Ziegler, J., C. Wu, P. Williams, C. White, B. Terreault, B. Scherzer, R. Schulte, E. Schneid,
    C. Magee, E. Ligeon, J. Ecuyer, W. Lanford, F. Kuehne, E. A. Kamykowski, W. Hofer,
    A. Guivarch, C. Filleux, V. Deline, J. C.A. Evans, B. Cohen, G. Clark, W. Chu, C. Bras-
    sard, R. Blewer, R. Behrisch, B. Appleton, and D. Allred (1978). Profiling hydrogen in
    materials using ion beams. *Nuclear Instruments and Methods in Physics Research 149*(1-
    3), 19–39.